RSC Advances

ROYAL SOCIETY OF CHEMISTRY

PAPER

View Article Online
View Journal | View Issue

Cite this: *RSC Adv.*, 2024, **14**, 11951

Flower-like Ag-decked non-stoichiometric Bi_2O_{3-x}/rGO hybrid nanocomposite SERS substrates for an effective detection of Rhodamine 6G dye molecules†

Awati Prema Mahadev,[a] C. Kavitha,[*a] Jil Rose Perutil,[b] Neena S. John[b] and H. C. Sudheeksha[c]

In early years, SERS-active substrates were generally noble metals. However, their practical applications were limited due to their poor biocompatibility, low uniformity and high cost. Recently, the utilization of semiconductor SERS-active substrates has greatly expanded the applications of SERS in many fields. However, metal-free SERS-active substrates have a low enhancement factor (EF), which can be overcome by adjusting their oxygen deficiency or through the effective preparation of non-stoichiometric semiconducting oxide materials. This is the key strategy and may work as an efficient and simple way to achieve high sensitivity and obtain an enhancement factor (*G*-factor) comparable to that of noble metals. Here, we report the preparation of flower-like rGO-Bi_2O_3/$Bi_2O_{2.75}$ and rGO-Ag-Bi_2O_3/$Bi_2O_{2.75}$ hybrid thin film nanocomposites using a liquid/liquid interface method (LLI) for the first time. In addition to the synergic effect of different enhancement mechanisms, the 3-D flower-like morphology of the substrate shows more favourable properties to improve the *G*-factor due to the existence of more hotspots. The rGO-Ag-Bi_2O_3/$Bi_2O_{2.75}$ hybrid thin-film nanocomposites show an EF of 1.8×10^9 with a detection ability of up to 1 nM towards Rhodamine 6G (R6G), which is highly toxic to humans and the aquatic environment.

Received 19th February 2024
Accepted 22nd March 2024

DOI: 10.1039/d4ra01286k

rsc.li/rsc-advances

1. Introduction

Surface enhanced Raman spectroscopy (SERS) is an ultrasensitive, highly specific analytical tool that has been widely used in food safety, environmental monitoring, medical diagnosis and treatment, and drug delivery monitoring.[1–15] SERS does not require complex sample pre-treatment compared to other analytical techniques such as mass spectrometry, polarography, and fluorescence spectroscopy. SERS is also preferred due to its high sensitivity, selectivity, and suitability for various analytical systems. The application of SERS as an analytical tool is mainly dependent on the use of an optimal substrate and its simple, effective preparation route. Although coinage nano-metals are primary SERS active materials, as they generate a strong electromagnetic field due to the strong surface plasmon resonance (SPR) effect, semiconductor-based SERS substrates are a new class of substrates with higher SERS uniformity, better chemical stability, biocompatibility and lower cost. The exploration of novel materials for multipurpose potential applications is a recent trend in research. Unlike metal SERS-active substrates, semiconductor-based SERS systems lack practical applications due to their poor EF and lower concentration detection ability, as the Raman signal enhancement solely depends on the chemical enhancement mechanism (CE). Recently, this matter has been addressed by researchers, and the presence of oxygen vacancies as defects and non-stoichiometric semiconductor metal oxide (MO) structures can improve the detection ability and enhancement factor. Detection levels as low as 10^{-7} M and even 10^{-8} M for α-MoO_{3-x} have been achieved.[16–18] The significant role of the distinct morphology of Ag loaded on a defect-rich MoO_3 sea urchin (Ag/SUMoO_3) SERS substrate was demonstrated as an *N*-nitrosodiphenylamine (NDPhA) sensor. The Ag/SUMoO_3 substrate exhibited an EF of 9.2×10^9 and could sense concentrations as low as 1 nM of 4-mercaptobenzoic acid (4-MBA) and 10^{-5} M NDPhA.[19] A sandwich substrate of Ag/analyte-methylene blue (MB) with defect-rich SUMoO_3 has been studied for the SERS detection of MB dye. An EF of 8.1×10^6 with detection of a concentration as low as 100 nM was achieved.[20] Hence, the preparation of a SERS substrate composed of plasmonic Ag and a defect-rich metal-oxide-decked rGO nanosheet could provide a SERS-active

[a]*Department of Chemistry R&D, Physics R&D, Centre for Advanced Materials Research, B.M.S. Institute of Technology & Management, An Autonomous Under Visvesvaraya Technological University, Bangalore 560064, India. E-mail: gkavitha21@bmsit.in*

[b]*Centre for Nano and Soft Matter Sciences, Shivanapura, Bengaluru 562162, India*

[c]*Horiba India Pvt. Ltd-IISc Industry Unit, Bangalore 560012, India*

† Electronic supplementary information (ESI) available. See DOI: https://doi.org/10.1039/d4ra01286k

substrate with improved EF and sensing power. The semiconductor chosen to prepare the rGO-based nanohybrid was Bi_2O_3. The semiconductor Bi_2O_3 exists in various crystalline phases, namely, α (monoclinic), β (tetragonal), γ (body-centred cubic), δ (face-centred cubic) ε (orthorhombic), ω (triclinic) and hexagonal phases[21] and non-stoichiometric phases including $Bi_2O_{2.7}$, $Bi_2O_{2.33}$, $Bi_2O_{2.75}$, and BiO_{2-x}.[22–24] Although bismuth oxide and its hybrids with carbon materials have well-known applications in photocatalysis and electrocatalysis, electrochemical energy storage systems, and biomedical fields,[25–28] there is only a single report exploring Bi_2O_3-based metal composites for SERS detection of environmental pollutants.[29] The SERS activity of reduced graphene oxide (rGO)-based Bi_2O_3 or its non-stoichiometric hybrid nanocomposites has not been investigated to date. Exploring the hybrid thin-film nanocomposites of rGO-Bi_2O_3/Bi_2O_{3-x} and Ag-incorporating rGO-Ag-Bi_2O_3/Bi_2O_{3-x} as SERS-active substrates will illuminate the choice of semiconductor-based SERS substrates for chemical sensors.

2. Materials and methods

2.1 Materials

The chemicals used were of analytical grade and were used without further purification. Graphite flakes (mesh size: 300), conc. sulphuric acid (H_2SO_4, 95%), conc. phosphoric acid (H_3PO_4, 85%), potassium permanganate ($KMnO_4$), hydrogen peroxide (H_2O_2, 30% w/v), hydrochloric acid (HCl, 35–36%), triethylamine ($(C_2H_5)_3N$), hydrazine hydrate ($NH_2 \cdot NH_2$), and acetone were purchased from Sigma Aldrich Chemicals Pvt. Ltd. Bismuth nitrate pentahydrate ($Bi(NO_3)_3 \cdot 5H_2O$, 98%) was purchased from Loba Chemie Pvt. Ltd. Tetraoctylammonium bromide (TOABr, 99%) was purchased from Otto Chemica Biochemica Reagents. Rhodamine 6G (R6G) was procured from SD Fine Chemicals Ltd. Double-distilled water and Milli-Q water were used for washing and all synthesis purposes, respectively.

2.2 Synthesis of graphene oxide

Graphite oxide was prepared using an improved modified Hummer's method.[30] Generally, in a 500 mL beaker, 1.0 g of graphite flakes were added to an acid mixture (90 mL : 10 mL) of conc. H_2SO_4 and H_3PO_4. The mixture was stirred using a magnetic stirrer to obtain a uniform solution. A 6.0 g of $KMnO_4$ was slowly added to the mixture while maintaining the temperature below 5 °C in an ice bath. The mixture was maintained at 45 ± 5 °C for 2 hours using a water bath. The beaker was shifted back to the ice bath, and 100 mL of deionized water was slowly added. The mixture was heated for 1 hour in a water bath at 80 °C. The oxidation reaction was terminated by adding 120 mL of deionized water and 15 mL of 30% H_2O_2. The solution was allowed to cool before being washed with a 9 : 1 ratio of deionized water and HCl. The solution was washed with distilled water several times until the acid was completely eliminated. The pH of the supernatant was checked before discarding it after each wash. The solution was filtered to obtain a viscous dark brown residue. The solid residue was dried in a hot air oven at 60 °C for 30 min to obtain graphite oxide. The graphite oxide was further sonicated for 45 min in Milli-Q water to convert it into exfoliated graphene oxide for further hybrid thin-film nanocomposite preparation.

2.3 Synthesis of rGO-Bi_2O_3/$Bi_2O_{2.75}$ and rGO-Ag-Bi_2O_3/$Bi_2O_{2.75}$ hybrid thin-film nanocomposites

The step-wise synthesis procedures for the rGO-Bi_2O_3/$Bi_2O_{2.75}$ and rGO-Ag-Bi_2O_3/$Bi_2O_{2.75}$ hybrid thin-film nanocomposites are presented in Fig. 1(a). The rGO-Bi_2O_3/$Bi_2O_{2.75}$ hybrid thin-film nanocomposites were prepared by employing the standard procedure using the liquid–liquid interface (LLI) method.[31] A 0.021 g of bismuth nitrate pentahydrate (22 mM, 2 mL) was added to 25 mL of Milli-Q water. A 1.88 mM solution of TOABr (phase transfer catalyst) in 25 mL of toluene (organic layer) was prepared. The precursor aqueous solution and toluene-containing phase transfer catalyst were mixed thoroughly using a separating funnel. The clear organic layer turned slightly cloudy, indicating the transfer of bismuth ions to the organic layer. Once metal precursors had phase-transferred to the organic layer, it was gently transferred to a 100 mL beaker containing 25 mL of a 5 mg mL^{-1} well-sonicated standard solution of GO and 1 mL of triethylamine. A 0.5 mL of hydrazine hydrate was carefully injected into the aqueous GO layer. The reaction mixture was heated in an oil bath at 90 °C for 1.5 hours. The thin film obtained at the liquid–liquid interface was collected on a glass, quartz, or silicon substrate as shown in Fig. 1(b) for various characterization studies. The thickness of the obtained rGO-Bi_2O_3/$Bi_2O_{2.75}$ hybrid thin-film nanocomposite was 15–20 μm.

The rGO-Ag-Bi_2O_3/$Bi_2O_{2.75}$ hybrid thin-film nanocomposites were synthesized similarly. Additionally, Ag^+ ions that were separately collected by phase-transferring 0.01 M $AgNO_3$ solution (in 5 mL Milli-Q water) to 4.755 mM of TOABr (in 5 mL toluene) were added to the toluene layer containing Bi^{3+} ions. Both toluene layers (Bi^{3+} and Ag^+) were mixed thoroughly and transferred to a 100 mL beaker containing 25 mL of a 5 mg mL^{-1} well-sonicated standard aqueous solution of GO and 1 mL of triethylamine. A 0.5 mL of hydrazine hydrate was injected carefully into the aqueous GO layer without disturbing the interface. The reaction mixture was heated in an oil bath at 90 °C for 1.5 hours. The thin film observed at the liquid–liquid interface after 1.5 hours was collected on the glass/quartz or silicon substrate as shown in Fig. 1(b). The thickness of the as-prepared rGO-Ag-Bi_2O_3/$Bi_2O_{2.75}$ hybrid thin-film nanocomposite was 10–18 μm.

The formation of rGO-Ag-Bi_2O_3/$Bi_2O_{2.75}$ using the LLI method occurs through *in situ* hydrolysis and reduction reactions.[32] The detailed reaction mechanism is shown in Fig. 1(c). The metal precursor, $Bi(NO_3)_3 \cdot 5H_2O$, hydrolyzes to bismuth hydroxide.[33] The bismuth ions thus formed are phase-transferred to the toluene layer using TOABr as a phase transfer catalyst (PTC). Similarly, silver nitrate, which is used as a metal precursor for silver ions, readily dissolves in water and is phase-transferred to toluene using PTC. Triethylamine [$(C_2H_5)_3N$] present in the aqueous layer acts as a hydrolyzing

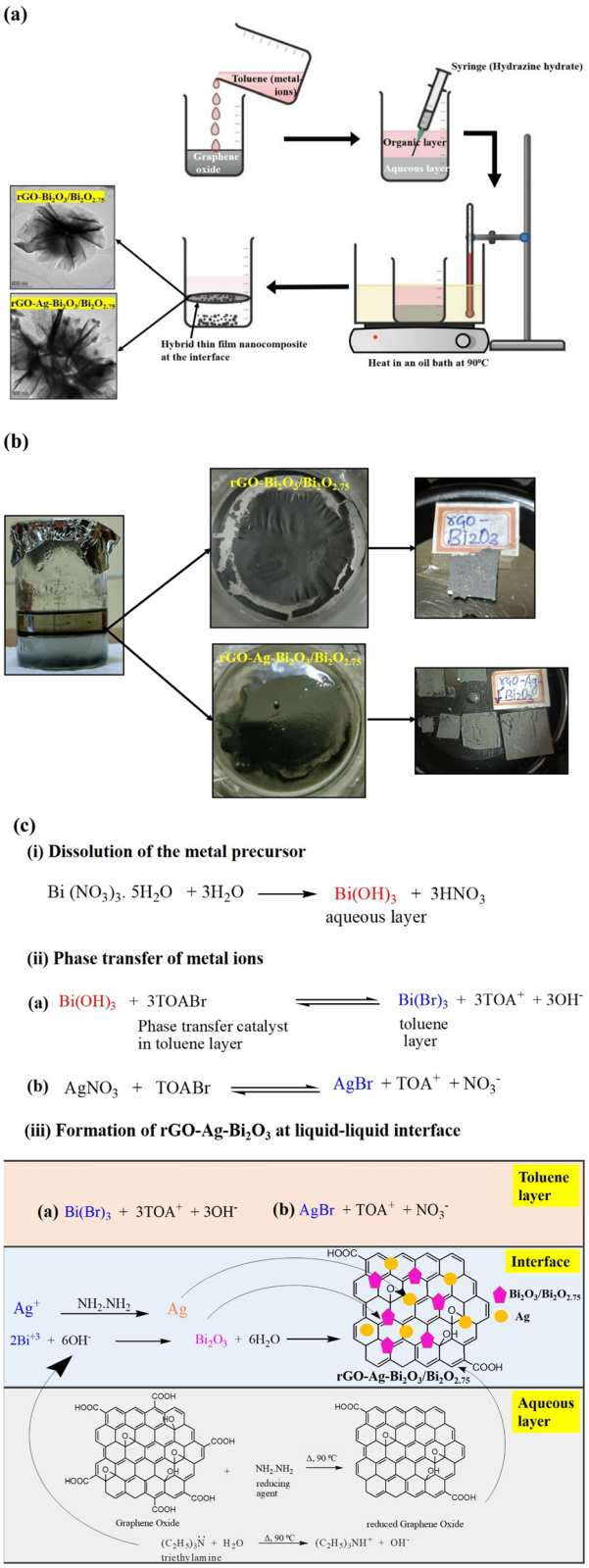

Fig. 1 (a) Step-wise schematic synthesis of rGO-Bi_2O_3/$Bi_2O_{2.75}$ and rGO-Ag-Bi_2O_3/$Bi_2O_{2.75}$ hybrid thin-film nanocomposites. (b) Photograph of the hybrid thin-film nanocomposite formation at the interface of liquids, top view of hybrid thin films and film samples collected on various substrates (left to right). (c) Step-wise reaction mechanism for the formation of rGO-Ag-Bi_2O_3/$Bi_2O_{2.75}$ hybrid thin-film nanocomposites.

agent and hydrolyzes Bi^{3+} ions to Bi_2O_3 at the interface.[34] Ag particles are formed *via in situ* reduction of Ag^+ ions by hydrazine hydrate (N_2H_4). Simultaneously, the graphene oxide (GO) is reduced to graphene oxide (rGO) by N_2H_4 injected into the aqueous layer. The stabilized thin film of rGO is formed at the interface on which Bi_2O_3 and Ag nanoparticles are anchored to form the rGO-Ag-Bi_2O_3 hybrid thin-film nanocomposites, as shown in Fig. 1(c). The formation of rGO-Bi_2O_3 at 90 °C was reported by Devi *et al.*[35] The possible formation of defects or oxygen vacancies is common in metal oxides synthesized using the LLI method. This is due to a lower temperature being employed in this LLI technique. The existence of defects and oxygen vacancies is necessary to enhance the SERS activity. However, annealing at a high temperature may result in a controlled metal oxide structure.

2.4 Characterization

The crystalline nature of hybrid thin-film nanocomposite samples was characterized using X-ray diffraction (XRD). The XRD patterns were recorded using a Rigaku Smart lab X-ray diffractometer with parallel beam optics, a 3 kW X-ray tube, a 9 kW rotating anode X-ray source, and Cu-Kα radiation (λ = 1.5418 Å, 40 kV, 30 mA). The presence of elements and their chemical oxidation states in the samples were confirmed using the XPS technique. The XPS survey scan and high-resolution XPS for both samples were recorded using the Thermo Scientific™ K-Alpha™ XPS system. FT-IR spectra were recorded for the prepared hybrid thin films collected on a silicon substrate using a PerkinElmer Spectrum 3. UV-vis absorbance spectra were recorded using a PerkinElmer Lambda 750 spectrophotometer. The morphology and elemental composition of the samples were obtained using a field emission scanning electron microscope (FESEM) (Apreo 2 S) coupled with a Thermo Fisher energy dispersive spectroscope (EDS) operated at an accelerating voltage range of 200 V to 30 kV and TESCAN and Bruker-MIRA 3 (FESEM) and Quantax 200 (EDS). Transmission electron microscopy (TEM), high-resolution transmission electron microscopy (HRTEM), and selected area electron diffraction (SAED) were conducted using a ThermoFisher Scientific-TALOS F200S G2 field emission transmission electron microscope (Camera 4K × 4K, In Column EDS detector) operated at an accelerating voltage of 200 kV. The thickness of the as-prepared thin film was determined by employing a DektaXT (Bruker) Surface Stylus Profilometer equipped with a stylus of 2 micron radius. The average step height was recorded for randomly selected area of both the nanocomposite thin films loaded on the glass substrate. The Raman/SERS spectra of the prepared hybrid samples and control experiments were recorded using a HORIBA LabRAM HR Evolution equipped with lasers of three wavelengths. All characterization data were analyzed using the Origin software.

2.5 SERS measurements

The SERS activity of rGO-Bi_2O_3/$Bi_2O_{2.75}$ and rGO-Ag-Bi_2O_3/$Bi_2O_{2.75}$ substrates were demonstrated using the dye R6G as a probe molecule, as it is a common fluorescent dye widely used

for SERS studies. A series of R6G dye solutions with a range of concentrations from 1 mM to 1 nM were prepared using the dilution method using Milli-Q water. A 20 μL of R6G was drop-cast sequentially on the as-prepared hybrid thin film substrates and allowed to dry. The SERS spectra of R6G adsorbed on the as-prepared hybrid thin-film nanocomposites, as well as on rGO- and $Bi_2O_3/Bi_2O_{2.75}$-only substrates, were recorded using a HORIBA LabRAM HR Evolution equipped with a 532 nm excitation laser. A 50× long working objective (NA = 0.5) was used to focus the laser and collect the scattered light in a back-scattering geometry. The system was calibrated before recording the spectra with the 520.7 cm^{-1} silicon peak as a reference. A Peltier-cooled charge-coupled device (CCD) linear array detector (1024 × 256 pixels) was used to detect the signal from a spectrograph with 600 grooves per mm grating. The system was controlled using the software LabSpec6. Data processing was further carried out using the same software. The typical Raman spectrum accumulation time for each spectrum was 1–10 seconds.

In this paper, we have demonstrated the use of rGO-$Bi_2O_3/Bi_2O_{2.75}$ and rGO-Ag-$Bi_2O_3/Bi_2O_{2.75}$ hybrid thin-film nanocomposites for SERS-based sensing applications. These substrates were prepared using a facile liquid/liquid interface (LLI) method to detect the dye Rhodamine 6G (R6G). To the best of our knowledge, this is the first time that non-stoichiometric metal oxide hybrid composites have been prepared using the LLI method. The crystalline phases and non-stoichiometric phases of the as-prepared nanohybrid films were confirmed using XRD. XPS analysis was used to ascertain the elemental chemical oxidation states in the hybrid thin-film nanocomposite samples. The optical properties of the rGO-$Bi_2O_3/Bi_2O_{2.75}$ and rGO-Ag-$Bi_2O_3/Bi_2O_{2.75}$ substrates were analyzed using Raman, FTIR, and UV spectroscopy. The morphology and uniform distribution of Ag-containing flower-like $Bi_2O_3/Bi_2O_{2.75}$ nanocomposites over rGO sheets were investigated and confirmed using SEM and TEM studies. SERS studies were performed for the rGO-$Bi_2O_3/Bi_2O_{2.75}$ and rGO-Ag-$Bi_2O_3/Bi_2O_{2.75}$ hybrid thin-film nanocomposites using R6G as an analyte. The rGO-$Bi_2O_3/Bi_2O_{2.75}$ hybrid thin-film nanocomposite substrate shows an EF of 7×10^4 due to the synergic effects of rGO and the non-stoichiometric metal oxide charge transfer effect. However, the further addition of a small amount of silver to the rGO-$Bi_2O_3/Bi_2O_{2.75}$ hybrid thin-film nanocomposites results in a huge EF of 1.8×10^9 and sufficient sensitivity to detect nearly 1 nM concentration of R6G. Detailed results and discussion, and the mechanism behind the SERS activity of the above-mentioned hybrid thin-film nanocomposites are discussed below.

3. Results and discussion

3.1 Structure of the samples

The crystallinity and non-stoichiometric phases of the synthesized hybrid thin-film nanocomposites were investigated using XRD studies as shown in Fig. 2. The diffraction peaks observed at Bragg angles (2θ) of 27.2°, ~30.0°, and 32.6° for both the samples are assigned to the (310), (222) and (321) planes of cubic (δ) Bi_2O_3, respectively (JCPDS no. 01-071-0467). An additional peak at 39.7° in the case of rGO-$Bi_2O_3/Bi_2O_{2.75}$ is assigned to the (024) plane of cubic (δ-Bi_2O_3). The peaks at 20°, 21.9°, ~24°, 25.4°, and ~35° can be indexed to the ($\bar{1}11$), (020), ($\bar{1}02$), (021) and ($\bar{2}12$) planes of monoclinic (α) Bi_2O_3 (JCPDS no. 00-041-1449). The peaks observed at 14.4° and ~47° in both the samples are attributed to the (002) and (200) planes of the non-stoichiometric oxide $Bi_2O_{2.75}$, and the small peaks at 56.8°, 68.5°, and 72.9° correspond to the (116), (220), and (109) planes of $Bi_2O_{2.75}$ (JCPDS no. 00-027-0049). After the incorporation of Ag in the sample, the hybrid thin-film nanocomposite also shows peaks at 38.1°, 44.2°, 64.5°, and 77.4°, which are characteristic peaks ascribed to the (111), (200), (220), and (311)

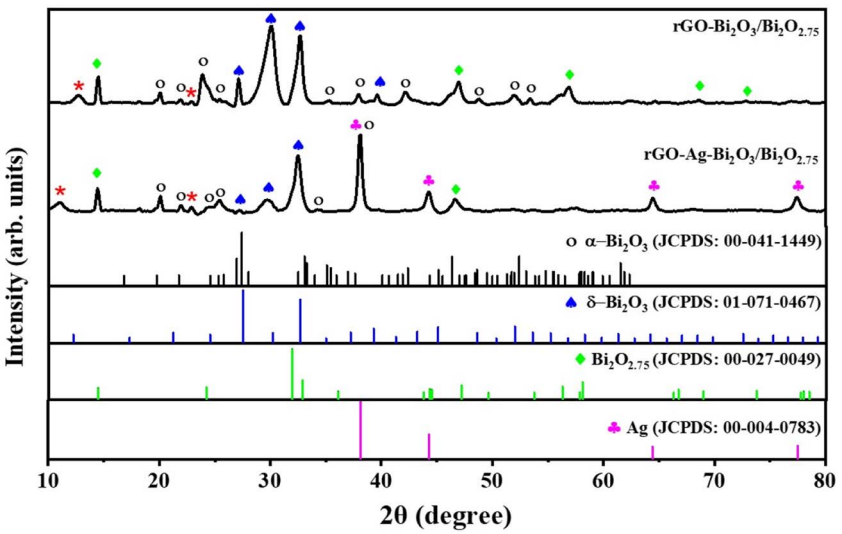

Fig. 2 XRD patterns of the as-prepared rGO-$Bi_2O_3/Bi_2O_{2.75}$ and rGO-Ag-$Bi_2O_3/Bi_2O_{2.75}$ hybrid thin-film nanocomposites along with JCPDS card numbers corresponding to α-Bi_2O_3, δ-Bi_2O_3, $Bi_2O_{2.75}$ and Ag for better understanding (top-bottom inside figure labels).

planes of cubic silver (JCPDS no. 00-004-0783). A small peak observed at $2\theta = 22.9°$ in both the samples is assigned to the rGO (002) plane, and the broad peak observed at 12.7° and 11.1° is due to the (001) plane of residual graphene oxide.[30] All the peaks belonging to α- and δ-Bi_2O_3, the non-stoichiometric phase $Bi_2O_{2.75}$, Ag peaks after its incorporation, and the rGO peak, confirmed the formation of non-stoichiometric rGO-Bi_2O_3/$Bi_2O_{2.75}$ and rGO-Ag-Bi_2O_3/$Bi_2O_{2.75}$ hybrid thin-film nanocomposites. The broad peaks in the XRD profile of the thin films indicate the polycrystalline nature of the samples. This is also confirmed and explained by TEM analysis later in this paper. The average crystallite size (D_{avg}) of both the hybrid thin-film nanocomposites were calculated using the Scherrer equation:

$$D_{avg} = 0.9\lambda/\beta \cos\theta \quad (1)$$

where $\lambda = 1.5406$ Å is the wavelength of the Cu-Kα target, θ is the Bragg diffraction angle, and β is the full width at half maximum (FWHM) of the selected diffraction peak. The calculated crystallite sizes varied in the range of 9–16 nm and 11–17 nm for rGO-Bi_2O_3/$Bi_2O_{2.75}$ and rGO-Ag-Bi_2O_3/$Bi_2O_{2.75}$, respectively, as shown in Table 1. The average crystallite sizes for rGO-Bi_2O_3/$Bi_2O_{2.75}$ and rGO-Ag-Bi_2O_3/$Bi_2O_{2.75}$ are ∼12 nm and ∼13 nm, respectively.

The surface chemical composition and chemical oxidation states of the elements present in the as-prepared hybrid thin-film nanocomposites were investigated through XPS survey scans and high-resolution XPS spectra. Fig. 3(a) shows XPS survey scans for rGO-Bi_2O_3/$Bi_2O_{2.75}$ (I) and rGO-Ag-Bi_2O_3/$Bi_2O_{2.75}$ (II), with prominent signature peaks corresponding to the presence of the elements Bi, C, and O in the rGO-Bi_2O_3/$Bi_2O_{2.75}$ and Bi, C, O, and Ag in rGO-Ag-Bi_2O_3/$Bi_2O_{2.75}$ hybrid thin-film nano composites. This confirms the absence of other elemental impurities in the sample.[25] The high-resolution XPS spectra for Bi 4f shown in Fig. 3(c) display two asymmetric peaks at 158.78 and 164.06 eV for rGO-Bi_2O_3/$Bi_2O_{2.75}$ and at 159.05 and 164.23 eV for rGO-Ag-Bi_2O_3/$Bi_2O_{2.75}$. These are attributed to Bi $4f_{5/2}$ and Bi $4f_{7/2}$, respectively, with a spin–orbit splitting value of 5.3 eV between the two asymmetrical peaks of Bi 4f, which has been reported in the literature, confirming the +3 oxidation state of Bi in both the samples.[36,37] After the incorporation of Ag in the rGO-Bi_2O_3 hybrid thin-film nanocomposite, additional peaks at higher binding energies of 160.2 eV (Bi $4f_{5/2}$) and 165.4 eV (Bi $4f_{7/2}$) were noted after deconvolution. These peaks arise due to the mild surface-charging effect due to the change in the polarization of crystals.[38] Fig. 3(d) presents the deconvoluted high-resolution XPS spectra of O 1s. In both the hybrid thin-film nanocomposites, the peaks were observed at 529.5 eV, 530.8 eV, and 532.3 eV (532.6 eV in rGO-Ag-Bi_2O_3/$Bi_2O_{2.75}$), which can be ascribed to the lattice oxygen of Bi_2O_3, surface oxygen vacancies or any oxygen species absorbed in the vacancies, and absorbed hydroxyl oxygen on the surfaces.[39] Similar O 1s peaks were observed for the rGO-Ag-Bi_2O_3/$Bi_2O_{2.75}$ hybrid thin-film nanocomposite, indicating the presence of the oxygen vacancies and surface defects. The O 1s peak component at 530.8 eV is substantial compared to the other resolved O 1s peaks and is ascribed to the presence of the oxygen vacancies in the non-stoichiometric Bi_2O_3/$Bi_2O_{2.75}$ lattice, which is also evident in the XRD pattern.[23] The oxygen vacancies in the semiconductor are one of the factors, along with the chemical enhancement and plasmonic effect of the metal, contributing to the SERS enhancement, as discussed in the upcoming section.[16,18] The two separate fitted peaks at 367.99 eV and 374.02 eV with an energy difference of around 6 eV as shown in Fig. 3(b) are characteristic of the Ag 3d metallic element state in the rGO-Ag-Bi_2O_3/$Bi_2O_{2.75}$ sample.[23] The deconvoluted XPS spectrum of C 1s for the rGO-Bi_2O_3/$Bi_2O_{2.75}$ hybrid thin-film nanocomposite is shown in Fig. 3(e). It shows three peaks centred at 284.8 eV (aromatic C=C/C–C), 286.3 eV (epoxide C–O) and 287.5 eV (–C=O, carbonyl group). The presence of the less-intense C–O of the epoxide and –C=O of the carbonyl group indicates less oxygen-bonded carbon due to the reduction of GO to rGO in the nanocomposites. Similar peak components were also observed in rGO-Ag-Bi_2O_3/$Bi_2O_{2.75}$ at 284.7 eV (aromatic C=C/C–C), 285.8 eV (epoxide C–O), and 286.6 eV (–C=O, carbonyl group).[25] The XPS measurement and XRD analysis of the as-prepared samples confirmed the formation of non-stoichiometric rGO-Bi_2O_3/$Bi_2O_{2.75}$ and rGO-Ag-Bi_2O_3/$Bi_2O_{2.75}$ hybrid thin-film nanocomposites.

Table 1 Crystallite sizes for the corresponding Bragg angles of rGO-Bi_2O_3/$Bi_2O_{2.75}$ and rGO-Ag-Bi_2O_3/$Bi_2O_{2.75}$ hybrid thin-film nanocomposites were calculated from XRD analysis

2θ	(hkl)	β (θ)	D (nm)
rGO-Bi_2O_3/$Bi_2O_{2.75}$			
23.96	$\bar{1}02$ (α-Bi_2O_3)	0.57	13.70
29.93	222 (δ-Bi_2O_3)	0.92	8.38
32.62	321 (δ-Bi_2O_3)	0.47	16.31
46.86	200 ($Bi_2O_{2.75}$)	0.69	10.54
56.75	116 ($Bi_2O_{2.75}$)	0.81	8.65
rGO-Ag-Bi_2O_3/$Bi_2O_{2.75}$			
32.44	321(δ-Bi_2O_3)	0.61	12.42
44.23	200 (Ag)	0.43	17.29
46.66	200 ($Bi_2O_{2.75}$)	0.57	12.89
64.42	220 (Ag)	0.45	14.85
77.39	311 (Ag)	0.55	11.27

3.2 Morphology of the samples

The surface morphologies of both the hybrid thin-film nanocomposites were analyzed using FESEM. The morphology and magnified SEM images of the rGO-Bi_2O_3/$Bi_2O_{2.75}$ and rGO-Ag-Bi_2O_3/$Bi_2O_{2.75}$ hybrid thin-film nanocomposites are shown in Fig. 4(a), (c), (b) and (d), respectively. The FESEM image of the rGO-Bi_2O_3/$Bi_2O_{2.75}$ nanocomposite shows flower-like nanostructures spread over the rGO sheet. The rGO sheet facilitates the formation of the nanostructure, as shown in pictures. It can be observed in Fig. 4(a) that the rGO sheets have manifested into a flower-like nanostructure after forming a composite with Bi_2O_3/$Bi_2O_{2.75}$, which otherwise generally appears as a wrinkled nanosheet, as marked in the FESEM image. The polycrystalline

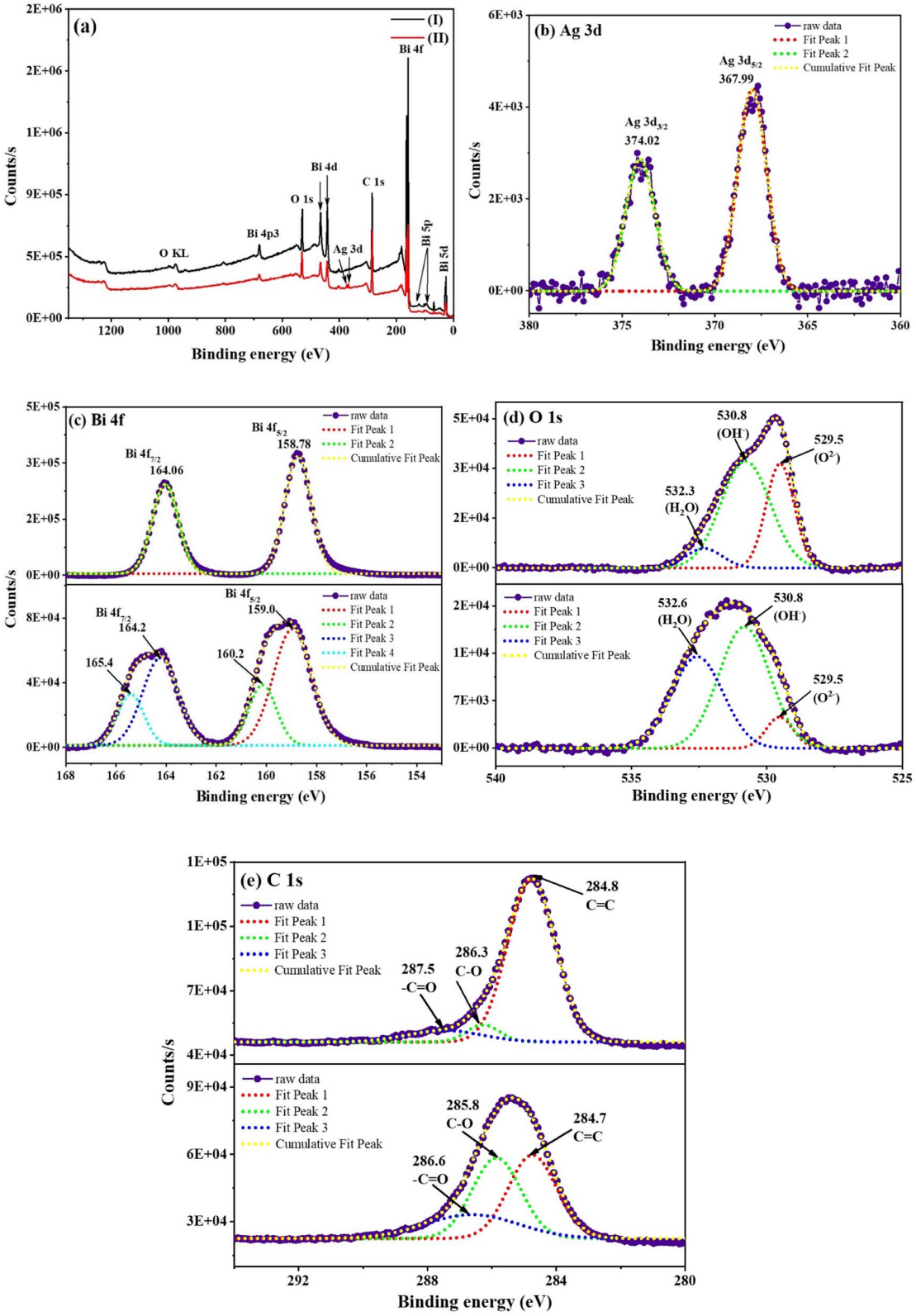

Fig. 3 (a) XPS survey scans of (I) rGO-Bi_2O_3/$Bi_2O_{2.75}$ and (II) rGO-Ag-Bi_2O_3/$Bi_2O_{2.75}$; high-resolution XPS spectra of (b) Ag 3d for rGO-Ag-Bi_2O_3/$Bi_2O_{2.75}$, (c) Bi 4f, (d) O 1s and (e) C 1s for rGO-Bi_2O_3/$Bi_2O_{2.75}$ (top) and rGO-Ag-Bi_2O_3/$Bi_2O_{2.75}$ (bottom) hybrid thin-film nanocomposites, respectively.

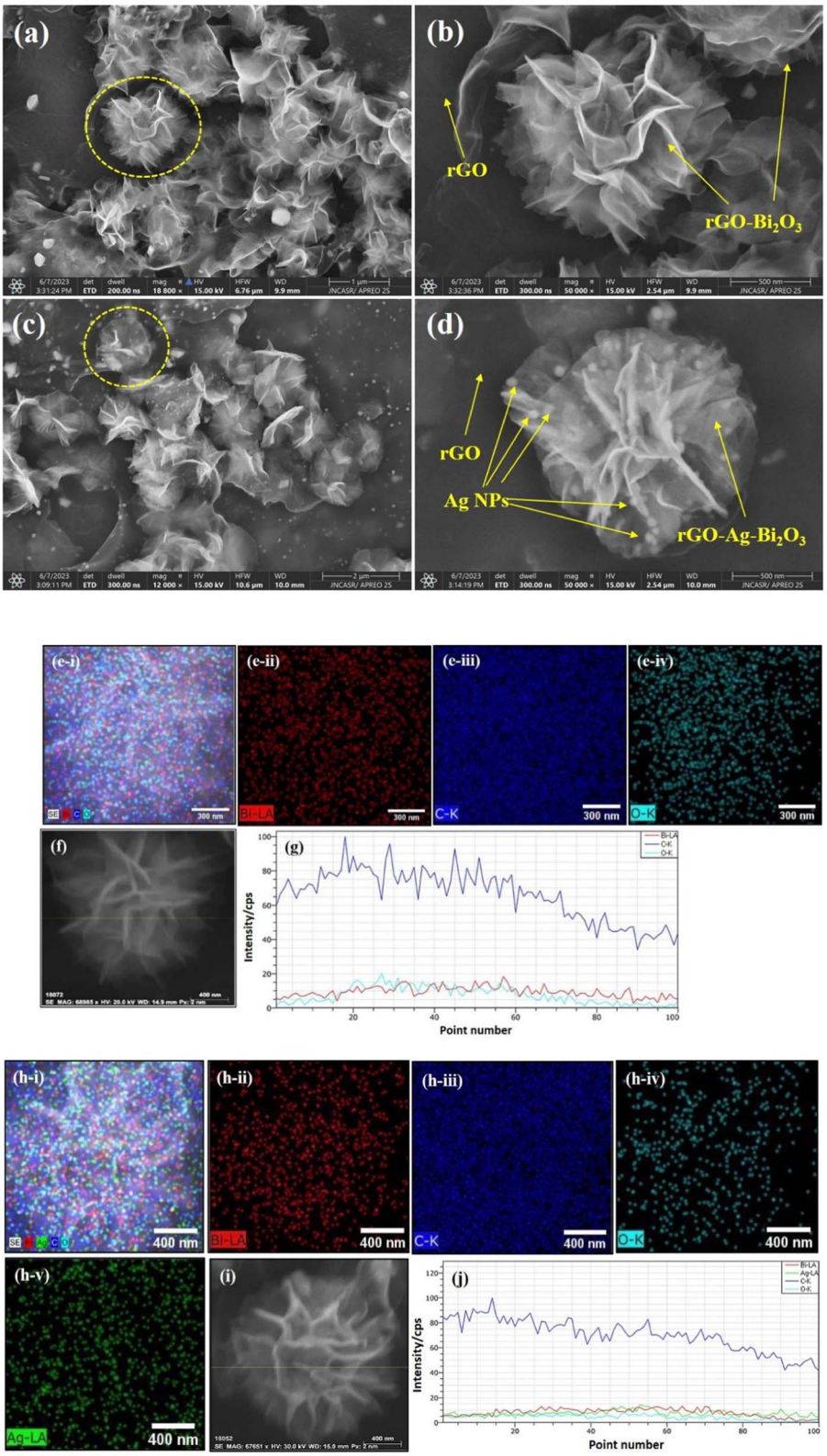

Fig. 4 FESEM images of the (a and b) rGO-Bi_2O_3/$Bi_2O_{2.75}$ and (c and d) rGO-Ag-Bi_2O_3/$Bi_2O_{2.75}$ hybrid thin-film nanocomposites, (e(i)) and (h(i)) elemental map overlay and (e(ii) to e(iv)) and (h(ii) to h(v)) individual elemental maps of the rGO-Bi_2O_3/$Bi_2O_{2.75}$ and rGO-Ag-Bi_2O_3/$Bi_2O_{2.75}$ hybrid thin film nanocomposites. (g) and (j): EDS line scan profile recorded along yellow line shown in (f) and (i) for the rGO-Bi_2O_3/$Bi_2O_{2.75}$ and rGO-Ag-Bi_2O_3/$Bi_2O_{2.75}$ hybrid thin-film nanocomposites, respectively.

nature of the formed structure with $Bi_2O_3/Bi_2O_{2.75}$ spread over rGO was observed. TEM analysis of $Bi_2O_3/Bi_2O_{2.75}$ of samples also showed similar observations, which are discussed below. In the case of the rGO-Ag-$Bi_2O_3/Bi_2O_{2.75}$ nanocomposite, after the incorporation of Ag, it was intriguing to observe a highly defined and distinguished morphology consisting of flower-like nanostructures of varied sizes. The distribution of $Bi_2O_3/Bi_2O_{2.75}$ with incorporated Ag NPs over an rGO sheet resulted in a compact shiny flower-like nanostructure. The Ag NPs appear as bright spots decorated over the flower petals, as presented in Fig. 4(d). The detailed elemental compositions of the synthesized rGO-metal-metal oxide thin films were further confirmed using elemental mapping. Fig. 4(e(i)) and (h(i)) shows the overall elemental composition of both the nanocomposites, respectively. Fig. 4(e(ii)) demonstrates that the element Bi is incorporated abundantly on the rGO sheet surface with densely distributed O (Fig. 4(e(iv))), indicating the formation of $Bi_2O_3/Bi_2O_{2.75}$. Moreover, major blue dots appear due to the element C present in the rGO sheets (Fig. 4(e(iii))). The elemental maps of a single flower-like nanostructure of rGO-Ag-$Bi_2O_3/Bi_2O_{2.75}$ shown in Fig. 4(h(ii)–(v)) indicate the presence of the four elements C, Bi, O, and Ag in the as-prepared hybrid thin-film nanocomposite structure. EDS line scans for single nanocomposite flowers were performed to explore the uniformity of the elemental composition and elemental distribution in the nanocomposite structures. Fig. 4(f) and (i) illustrate the SEM images of selected flower structures used for EDS line mapping, and scan lines are shown as yellow lines. As shown in Fig. 4(g) and (j), EDS line profiles for both the nanocomposites show a greater intensity of C, which is also obvious in the elemental mapping [Fig. 4(e) and (h)]. The line scan profile shows a homogenous distribution of C, Bi and O in the rGO-$Bi_2O_3/Bi_2O_{2.75}$ and Bi, C, Ag, and O in rGO-Ag-$Bi_2O_3/Bi_2O_{2.75}$ nanocomposites. These results are consistent with the EDS mapping [Fig. 4(e) and (h)] and TEM EDS analysis [Fig. 7(a) and (c)], which will also be discussed below. The extended line profile of C comes from the existence of the rGO sheet beneath or surrounding the nanoflower. The intensity of the EDS line profiles of Bi, O, and Bi, O and Ag in the respective nanoflowers are very similar and indicate the proper merging of $Bi_2O_3/Bi_2O_{2.75}$ or Ag-$Bi_2O_3/Bi_2O_{2.75}$ with rGO to form the rGO-$Bi_2O_3/Bi_2O_{2.75}$ and rGO-Ag-$Bi_2O_3/Bi_2O_{2.75}$ nanocomposites. Hence, morphological details confirmed the formation of the rGO-

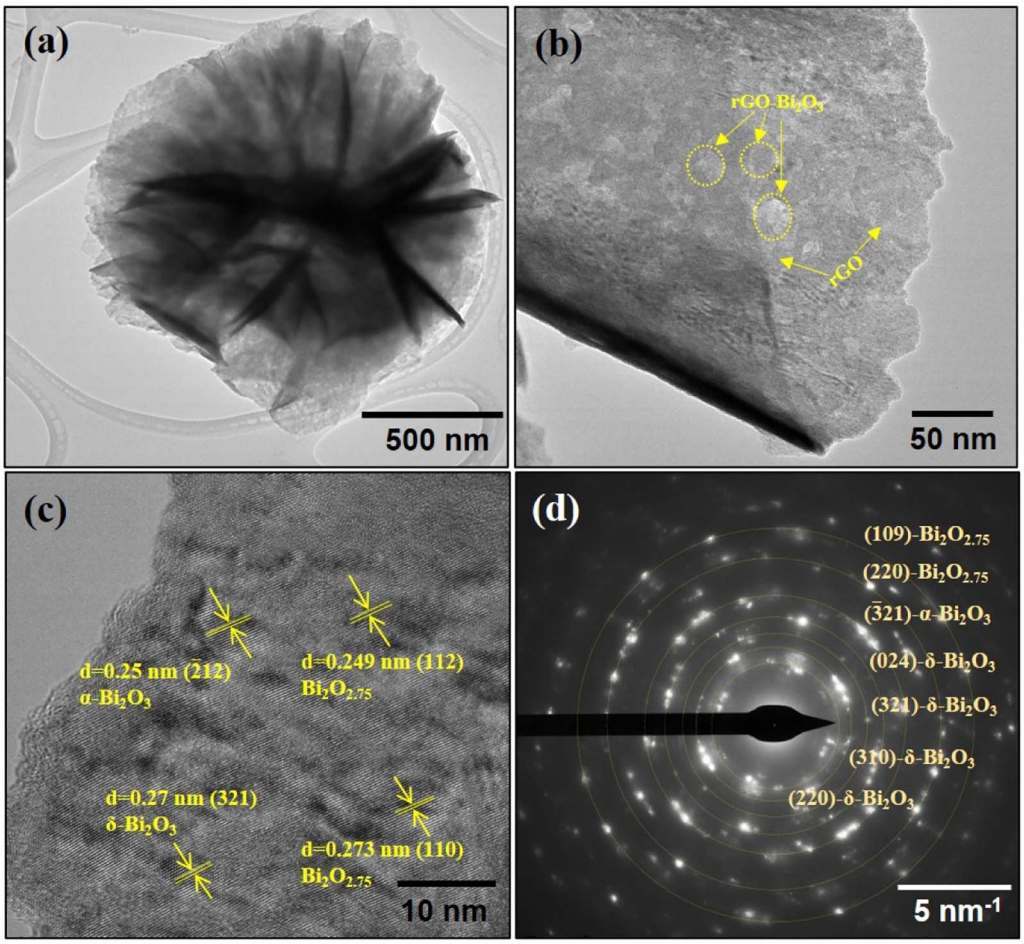

Fig. 5 (a) TEM image of an rGO-$Bi_2O_3/Bi_2O_{2.75}$ nanoflower. (b) Magnified view of an rGO-$Bi_2O_3/Bi_2O_{2.75}$ nanoflower petal. (c) HRTEM image and (d) SAED profile of rGO-$Bi_2O_3/Bi_2O_{2.75}$ hybrid thin-film nanocomposite.

metal-metal oxide hybrid thin-film nanocomposites over the rGO sheet.

The TEM analysis further supports the nanostructure details of the rGO-Bi_2O_3/$Bi_2O_{2.75}$ nanoflower, as shown in Fig. 5(a and b). The crystalline and amorphous regions are clearly shown in the magnified view of the nanoflower petal and are highlighted in Fig. 5(b). The HRTEM image shown in Fig. 5(c) presents the distinct regions of the hybrid thin film formed by the α- and δ-Bi_2O_3/$Bi_2O_{2.75}$. The processed HRTEM image showed lattice fringes with inter-planar distances of 0.25 nm ($\bar{2}12$-α-Bi_2O_3), 0.27 nm (321-δ-Bi_2O_3), 0.249 nm (112-$Bi_2O_{2.75}$), and 0.273 nm (110-$Bi_2O_{2.75}$), as highlighted in Fig. 5(c). The polycrystallinity of the nanocomposite was also evident in the SAED profile, as shown in Fig. 5(d). The SAED profile shows the characteristic planes of α-Bi_2O_3 ($\bar{3}21$), δ-Bi_2O_3 (024), (321), (310) and $Bi_2O_{2.75}$ (109) and (220), implying the formation of non-stoichiometric metal oxide hybrids with the rGO nano sheet. The TEM image of rGO-Ag-Bi_2O_3/$Bi_2O_{2.75}$ presents a similar flower-like morphology consisting of well-anchored Ag NPs over the nanostructure, as shown in Fig. 6(a). The black dots marked in Fig. 6(b) show the Ag NPs decorated over the nano flower petal. The HRTEM image of rGO-Ag-Bi_2O_3/$Bi_2O_{2.75}$ presented in Fig. 6(c) shows a magnified view of the rGO nanocomposite with α- and δ-Bi_2O_3/$Bi_2O_{2.75}$, and the Ag NPs decorated over it. The FFT process of the selected area showed inter-planar distances of 0.25 nm ($\bar{2}12$-α-Bi_2O_3), 0.23 nm (024-δ-Bi_2O_3), 0.16 nm (116-$Bi_2O_{2.75}$) and 0.236 nm corresponding to Ag (111), as illustrated in Fig. 6(c). The SAED pattern shown in Fig. 6(d) revealed the polycrystalline nature and few characteristic planes of α-Bi_2O_3 ($\bar{3}21$), δ-Bi_2O_3 (220, 310), $Bi_2O_{2.75}$ (220) and Ag (220, 311), strongly indicating the formation of rGO-Ag-Bi_2O_3/$Bi_2O_{2.75}$ hybrid thin-film nanocomposites. The FESEM images (Fig. 4) show rGO nanosheets, but in the TEM images, it is difficult to distinguish as rGO and its hybrid have sheet-like structures; hence, the lattice fringes corresponding to Bi_2O_3/$Bi_2O_{2.75}$ and Ag are presented in the HRTEM images. The elemental composition of the synthesized samples was investigated using TEM-EDS and is presented in Fig. 7(a) and (c). The substantial presence of O and Bi in rGO-Bi_2O_3/$Bi_2O_{2.75}$ and O, Bi, and Ag in rGO/Ag-Bi_2O_3/$Bi_2O_{2.75}$, along with C, was noted. The average size of the flower-like structures obtained *via* TEM studies is 4.64 μm for rGO-Bi_2O_3/$Bi_2O_{2.75}$ and 0.705 μm for rGO-Ag-Bi_2O_3/$Bi_2O_{2.75}$ (Fig. 7(b) and (d)); they are composed of small rGO-Bi_2O_3/$Bi_2O_{2.75}$ and rGO-Ag-Bi_2O_3/$Bi_2O_{2.75}$ crystallites of various sizes as mentioned in

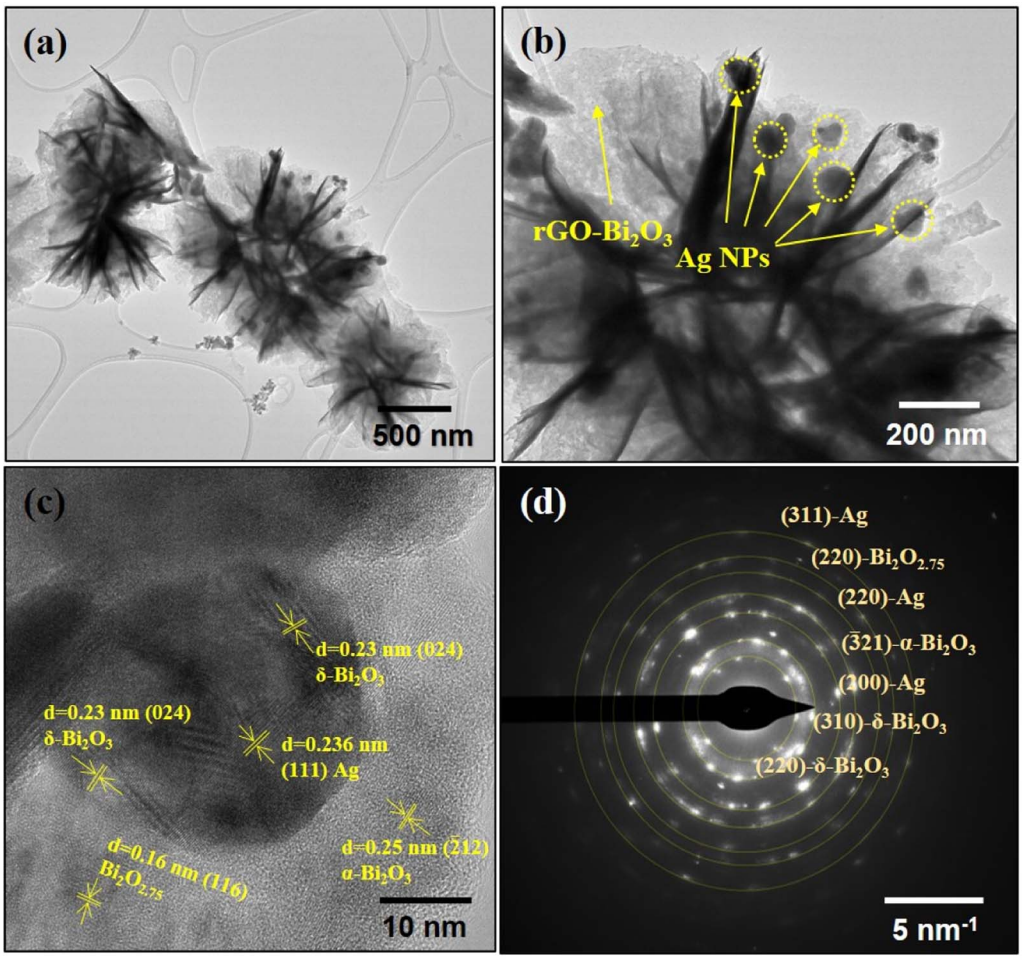

Fig. 6 (a) TEM image of an rGO-Ag-Bi_2O_3/$Bi_2O_{2.75}$ nanoflower (b) Magnified view of rGO-Ag-Bi_2O_3/$Bi_2O_{2.75}$ nanoflower petals. (c) HRTEM image of an rGO-Ag-Bi_2O_3/$Bi_2O_{2.75}$ hybrid thin-film nanocomposite. (d) SAED pattern of the rGO-Ag-Bi_2O_3/$Bi_2O_{2.75}$ hybrid thin-film nanocomposite.

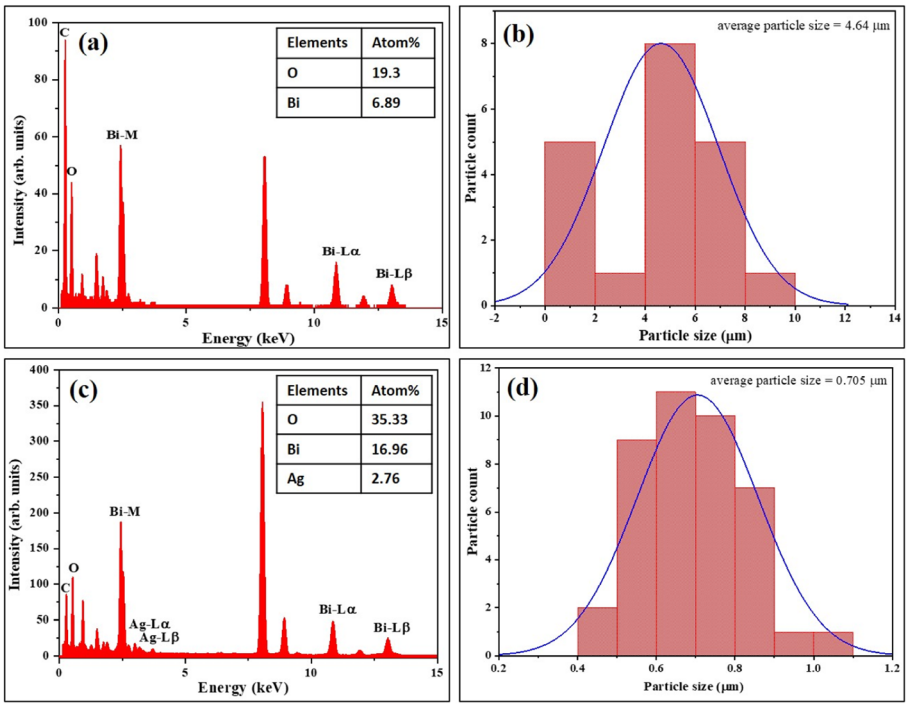

Fig. 7 EDS analysis and particle size distribution histogram of the (a and b) rGO-Bi_2O_3/$Bi_2O_{2.75}$ and (c and d) rGO-Ag-Bi_2O_3/$Bi_2O_{2.75}$ hybrid thin-film nanocomposites.

Table 1. The difference in average sizes among the hybrid thin-film nanocomposites justifies the SEM morphology observation. As shown in SEM analysis, the morphology of rGO-Bi_2O_3/$Bi_2O_{2.75}$ is more dispersed, non-uniform, and agglomerated, and hence, the particle size is large as compared to that of rGO-Ag-Bi_2O_3/$Bi_2O_{2.75}$, for which the particles were more defined, compact and of smaller size (see Fig. 4(a) and (c)). This further confirms the slight change in the morphology of the nanocomposite after introducing the Ag NPs.

3.3 Optical properties of the samples

FTIR analysis of the samples was further performed to identify functional groups present in the synthesized hybrid thin-film nanocomposites. The FTIR spectra for rGO-Bi_2O_3/$Bi_2O_{2.75}$ and

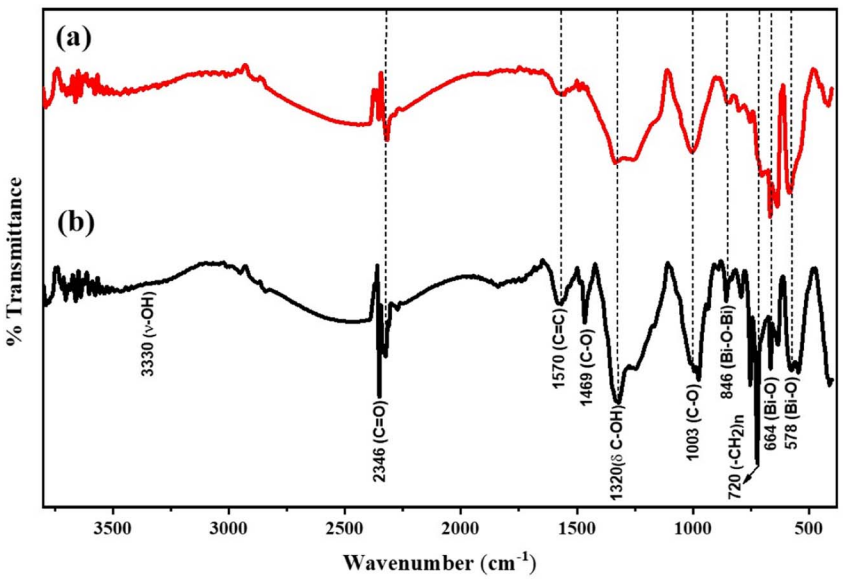

Fig. 8 FTIR spectra of the as-synthesized (a) rGO-Bi_2O_3/$Bi_2O_{2.75}$ and (b) rGO-Ag-Bi_2O_3/$Bi_2O_{2.75}$ hybrid thin-film nanocomposites.

its plasmonic composite, rGO-Ag-Bi_2O_3/$Bi_2O_{2.75}$, are shown in Fig. 8. In both cases, a broad spectrum at ~3330 cm^{-1} was observed due to the –OH stretching vibration of water molecules adsorbed on the hybrid thin-film nanocomposites. A characteristic small peak at 846 cm^{-1} corresponds to the Bi–O–Bi stretching in Bi_2O_3 units. The sharp peak at 664 cm^{-1} and broad shoulder at 578 cm^{-1} indicate the Bi–O stretching vibration of Bi_2O_3. The minor peaks observed at 1003, 1570, and 2346 cm^{-1} correspond to the epoxy or alkoxy C–O stretching mode, C=C stretching mode of the skeletal vibration of rGO, and C=O stretching mode, respectively.[40] The broad peak observed at 1320 cm^{-1} corresponds to the C–OH bending.[41] In the case of rGO-Ag-Bi_2O_3/$Bi_2O_{2.75}$, the peaks observed at 720 cm^{-1} and 1469 cm^{-1} are ascribed to the $(CH_2)_n$ bending vibration[42] and C–O stretching mode.[40] The absence or presence of very weak signals at signature vibrational frequencies for oxygen-containing functional groups like C=O, –OH, and –C–O–C– indicate the complete reduction of graphene oxide, and the presence of a characteristic metal–oxygen bond between 600 and 1000 cm^{-1} implies the formation of rGO-Bi_2O_3/$Bi_2O_{2.75}$ and its plasmonic hybrid rGO-Ag-Bi_2O_3/$Bi_2O_{2.75}$ thin film.[43]

The optical properties of the as-synthesized samples were studied using UV-vis spectroscopy. The UV-vis spectra of rGO-Bi_2O_3/$Bi_2O_{2.75}$ and rGO-Ag-Bi_2O_3/$Bi_2O_{2.75}$ are shown in Fig. 9(a) and (b). The absorptions observed at 263 nm and 279 nm in rGO-Bi_2O_3/$Bi_2O_{2.75}$ and rGO-Ag-Bi_2O_3/$Bi_2O_{2.75}$, respectively, are the characteristic absorbance of π–π* transitions in the aromatic C=C bonds of rGO, which indicates a reduction of GO to rGO and restoration of the electronic conjugation in graphene sheets.[44] The absorption edge of Bi_2O_3 was observed at around 470 nm in both nanohybrids, as reported previously.[45] The rGO-Bi_2O_3/$Bi_2O_{2.75}$ shows absorption in the visible range, which could be associated with free electrons or small polarons originating due to the oxygen vacancies. Similar plasmonic resonances are typical in non-stoichiometric metal oxides and derivatives with oxygen vacancies or defects.[22,46] The UV-vis spectra for rGO-Ag-Bi_2O_3/$Bi_2O_{2.75}$ showed enhanced wide absorbance in the visible range and localized surface plasmon resonance (LSPR) at 450–550 nm. This is observed due to the oxygen vacancies and strong electronic coupling between the Ag NPs present in the Ag-Bi_2O_3/$Bi_2O_{2.7}$ matrix.[46,47]

Important features of GO and rGO, such as their defect sites, crystallinity, layers, and types of functional groups containing oxygen can be explored using their Raman spectra.[48,49] Raman analysis also helps in interpreting the reduction of graphite oxide layers, *i.e.*, the conversion of functional groups like hydroxyl groups to epoxy groups. In the LLI synthesis, there is *in situ* conversion of GO to rGO by hydrazine hydrate. The Raman spectra of as-synthesized rGO, rGO-Bi_2O_3/$Bi_2O_{2.75}$, and rGO-Ag-Bi_2O_3/$Bi_2O_{2.75}$ are shown in Fig. S1.† The two signature D and G bands of rGO at 1342 cm^{-1} and 1581 cm^{-1} respectively can be seen in the spectra in Fig. S1(a).† The A_{1g} mode D band can be observed at 1342 cm^{-1} for rGO and rGO-Bi_2O_3/$Bi_2O_{2.75}$, as well as at 1330 cm^{-1} for rGO-Ag-Bi_2O_3/$Bi_2O_{2.75}$. It appears because of the disordered graphite planar structure, the vibrational stretching of sp^3-hybridized C–C bonds, and the breathing mode of free bonds belonging to terminal aromatic rings. The high intensity of the D band peak corresponds to the degree of structural defects or edges.[50] The first-order scattering arising due to E_{2g} phonon modes in the Brillouin zone at the K point, *i.e.*, the G-band, can be observed at 1581 cm^{-1} for rGO and rGO-Ag-Bi_2O_3/$Bi_2O_{2.75}$, as well as at higher wavenumber for rGO-Bi_2O_3/$Bi_2O_{2.75}$, *i.e.*, 1590 cm^{-1}. This is a characteristic peak of the sp^2-hybridized carbon atoms of graphitic aromatic layers and stretching of C=C bonds in the aromatic rings and chains. The D and G bands are wider due to the oxidation of graphite and its lattice deformation.

The Raman spectra also show second-order bands at ~2500–3300 cm^{-1} corresponding to second-order phonon vibrations. A broader 2D peak is observed at a higher wavelength of 2929 cm^{-1} for rGO, which corresponds to the layered structure of graphite oxide.[51,52] The higher intensity of the 2D band in rGO-Bi_2O_3/$Bi_2O_{2.75}$ and rGO-Ag-Bi_2O_3/$Bi_2O_{2.75}$ indicates the presence of a more secluded graphene area, deintercalated rGO sheets out of packed multilayer GO sheets and elimination of oxygen groups.[53,54] The degree of disorder among carbon-containing samples can be estimated by the relative intensity ratio (I_D/I_G). The intensity ratios calculated for rGO, rGO-Bi_2O_3/$Bi_2O_{2.75}$, and rGO-Ag-Bi_2O_3/$Bi_2O_{2.75}$ are 1.11, 1.09, and 1.14, respectively. No significant difference was noted in the intensity ratios of rGO and rGO-Bi_2O_3/$Bi_2O_{2.75}$, indicating reinstatement of sp^2 domains and formation of sp^2 carbon after reduction.

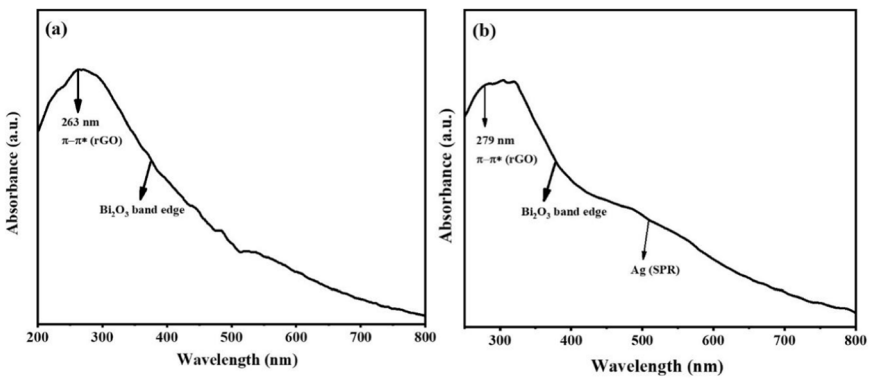

Fig. 9 UV-vis spectra of (a) rGO-Bi_2O_3/$Bi_2O_{2.75}$ and (b) rGO-Ag-Bi_2O_3/$Bi_2O_{2.75}$ hybrid thin-film nanocomposites.

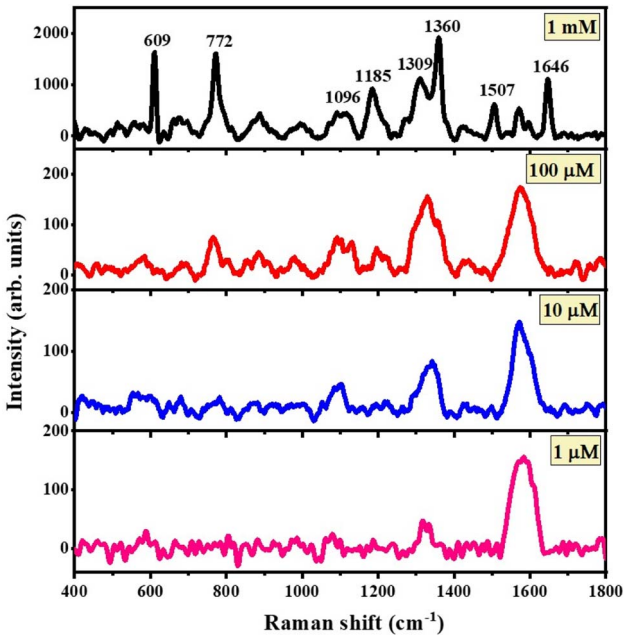

Fig. 10 SERS spectra for concentrations of 1 mM to 1 μM R6G adsorbed on the rGO-Bi_2O_3/$Bi_2O_{2.75}$ hybrid thin-film nanocomposites.

However, a small increase in the intensity ratio of rGO-Ag-Bi_2O_3/$Bi_2O_{2.75}$ as compared to those of rGO and rGO-Bi_2O_3/$Bi_2O_{2.75}$ indicates the formation of a more disordered layered graphitic structure after the deposition of Ag and Bi_2O_3/$Bi_2O_{2.75}$ on rGO.[53] As shown in Fig. S1† (inset), the characteristic Raman peaks for Bi_2O_3/$Bi_2O_{2.75}$ were observed at ~262 cm^{-1}, 288 cm^{-1}, 307 cm^{-1}, 328 cm^{-1}, 412 cm^{-1}, 440 cm^{-1}, 462 cm^{-1}, 527 cm^{-1}, and 546 cm^{-1} in the case of the rGO-Bi_2O_3/$Bi_2O_{2.75}$ hybrid thin-film nanocomposite, whereas similar peaks along with those for Ag at 440 cm^{-1} and 562 cm^{-1} were observed for the rGO-Ag-Bi_2O_3/$Bi_2O_{2.75}$ hybrid nanocomposite. The peaks at ~262 cm^{-1}, 288 cm^{-1}, 307 cm^{-1}, 328 cm^{-1}, 412 cm^{-1}, 440 cm^{-1}, and 462 cm^{-1}, can be assigned to α-Bi_2O_3, whereas those at 527 cm^{-1} and 546 cm^{-1} were assigned to the presence of $Bi_2O_{2.75}$ in the rGO-Bi_2O_3/$Bi_2O_{2.75}$ and rGO-Ag-Bi_2O_3/$Bi_2O_{2.75}$ hybrid thin-film nanocomposites.[55,56] Peaks at 442 cm^{-1} and 562 cm^{-1} are noted in the case of rGO-Ag-Bi_2O_3/$Bi_2O_{2.75}$ due to the incorporation of the Ag NPs.[57]

3.4 SERS application

The SERS properties of the rGO-Bi_2O_3/$Bi_2O_{2.75}$ and rGO-Ag-Bi_2O_3/$Bi_2O_{2.75}$ hybrid thin-film nanocomposites were studied using R6G as a probe molecule. As shown in Fig. 10, the SERS spectra for rGO-Bi_2O_3/$Bi_2O_{2.75}$ indicate the detection ability of the rGO-Bi_2O_3/$Bi_2O_{2.75}$ hybrid thin film towards the analyte R6G

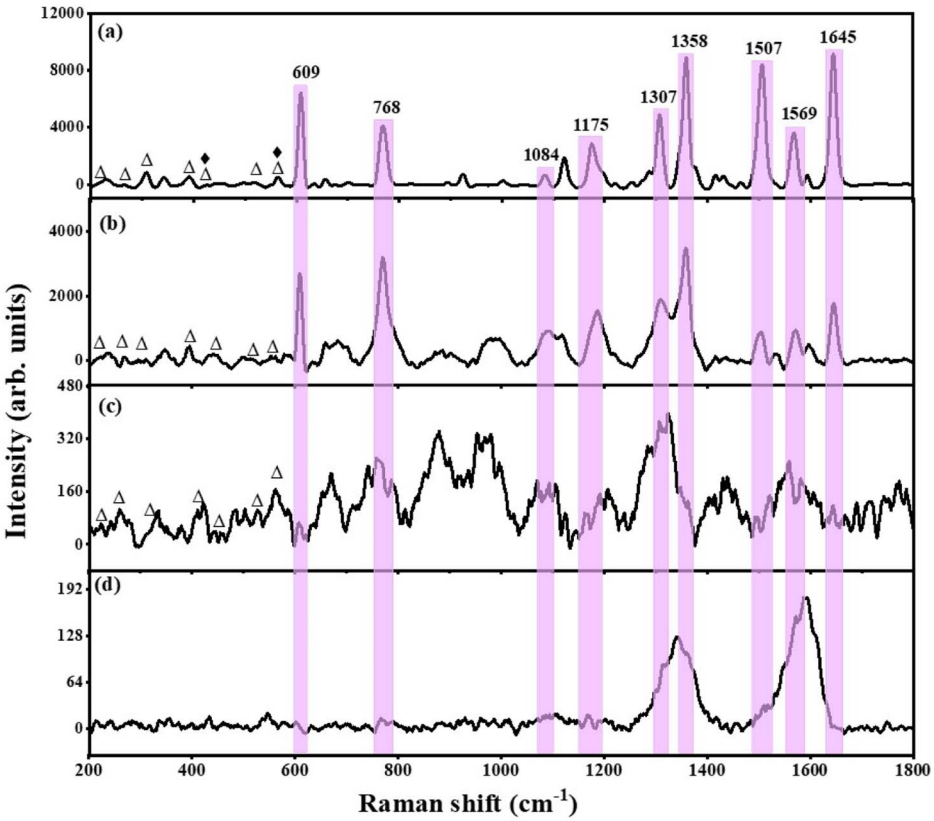

Fig. 11 Comparison of the SERS spectra for the detection of 1 mM R6G using the (a) rGO-Ag-Bi_2O_3/$Bi_2O_{2.75}$ and (b) rGO-Bi_2O_3/$Bi_2O_{2.75}$ hybrid thin-film nanocomposites and (c) Bi_2O_3/$Bi_2O_{2.75}$ and (d) rGO thin films. The 'Δ' here represents Raman peaks of Bi_2O_3/$Bi_2O_{2.75}$ and '◆' represents Raman signals of Ag. The shaded areas highlight the characteristic peaks of R6G.

from 1 mM to 1 μM. It can be observed in the SERS profile that the characteristic peaks of R6G are present but feeble for the lower concentration of 10 μM and very poor for 1 μM of R6G; this indicates the ability of rGO-Bi_2O_3/$Bi_2O_{2.75}$ to detect concentrations down to 10 μM of R6G.

To understand the extent of the SERS activity, control SERS experiments were performed on the metal oxides alone, *i.e.*, Bi_2O_3/$Bi_2O_{2.75}$, and rGO individually, towards 1 mM R6G and compared with those of the as-prepared hybrid thin-film nanocomposites. The comparative SERS activity of the rGO-Ag-Bi_2O_3/$Bi_2O_{2.75}$, rGO-Bi_2O_3/$Bi_2O_{2.75}$, Bi_2O_3/$Bi_2O_{2.75}$, and rGO substrates is shown in Fig. 11. It is observed that the characteristic peaks of R6G appear most prominent in the case of rGO-Ag-Bi_2O_3/$Bi_2O_{2.75}$. As mentioned earlier, the other small peaks at ~223 cm^{-1}, 268 cm^{-1}, 308 cm^{-1}, 393 cm^{-1}, and 445 cm^{-1} are the Raman-active signals of Bi_2O_3, whereas those at ~526 cm^{-1} and ~566 cm^{-1} are observed due to the presence of $Bi_2O_{2.75}$. In the case of rGO-Ag-Bi_2O_3/$Bi_2O_{2.75}$, the Raman peaks at 440 cm^{-1} and 566 cm^{-1} represent the co-existence of $Bi_2O_{2.75}$ and Ag.[22,54–56] The greater intensity of the R6G SERS signals could be due to a combined effect originating due to the electromagnetic effect exhibited by the Ag NPs and chemical enhancement by the rGO-MO system due to the presence of the oxygen vacancies caused by the existence of non-stoichiometric $Bi_2O_{2.75}$ in the rGO-Ag-Bi_2O_3/$Bi_2O_{2.75}$ hybrid thin-film nanocomposites. In addition, a surface enhanced resonance Raman spectroscopy (SERRS) contribution may be expected from R6G, especially under 532 nm laser excitation. The flat background of the Raman spectra in the hybrid composites must be due to the fluorescence-quenching nature of rGO.

The addition of a small amount of Ag to the rGO-Bi_2O_3/$Bi_2O_{2.75}$ hybrid thin-film nanocomposite provided a huge enhancement in the Raman signal of the analyte at a concentration of 1 mM. Hence, it was decided to further explore the SERS activity of the hybrid substrate for lower concentrations of R6G. It is clear from Fig. 12 that the rGO-Ag-Bi_2O_3/$Bi_2O_{2.75}$ hybrid substrate showed significantly improved sensitivity toward 1 mM R6G compared to the rGO-Bi_2O_3/$Bi_2O_{2.75}$ hybrid thin-film nanocomposite and was able to detect lower R6G concentrations down to 1 nM. The Raman bands of the analyte R6G are observed clearly down to 1 nM, as shown in Fig. 12. The signature Raman bands of rGO at 1342 cm^{-1} and 1590 cm^{-1} for the D- and G-bands, respectively, are denoted with asterisks. The signature peaks of R6G adsorbed on the rGO-Ag-Bi_2O_3/$Bi_2O_{2.75}$ substrate are well-defined and prominent. The enhanced Raman signals assigned to R6G were observed at around 609 cm^{-1} and 769 cm^{-1} and correspond to the bending vibration mode of the C–C–C ring in the plane and C–H out of the plane of the xanthene skeleton, respectively. The Raman signals at 1084 cm^{-1} and 1175 cm^{-1} are correlated to the C–H out-of-plane bending vibration and C–C stretching vibrations, respectively. The peaks at 1307 cm^{-1}, 1358 cm^{-1}, 1507 cm^{-1}, 1569 cm^{-1}, and 1645 cm^{-1} correspond to the C–C in-plane stretching vibrations of the aromatic rings.[58,59] The enhanced R6G Raman bands at 609 cm^{-1}, 768 cm^{-1}, and 1084 cm^{-1} can be observed at concentrations as low as 1 nM with very low intensity. For further clarity, an enlarged view of the R6G Raman bands at nanomolar concentrations on rGO-Ag-Bi_2O_3/$Bi_2O_{2.75}$ is plotted in Fig. S2.† In Fig. S2,† the R6G Raman bands are clearly visible down to 1 nM. This is attributed to the electromagnetic enhancement effect of Ag along with the synergic effects of the other enhancement mechanisms, which were discussed earlier.

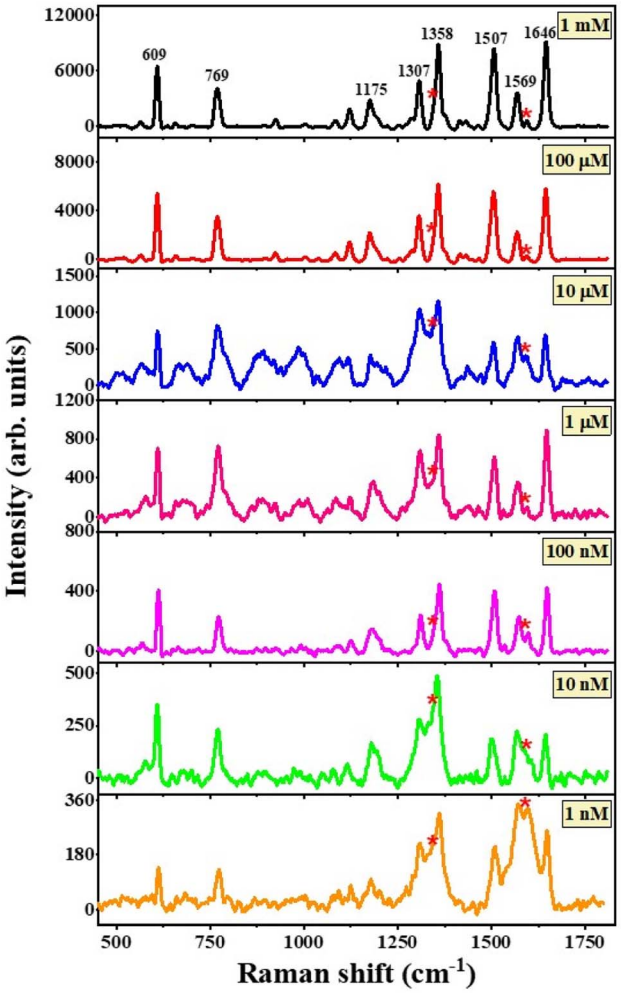

Fig. 12 SERS spectra for concentrations from 1 mM to 1 nM of R6G adsorbed on the rGO-Ag-Bi_2O_3/$Bi_2O_{2.75}$ hybrid thin-film nanocomposites. The asterisks represent the D- and G-bands of rGO.

The linear dependence of the intensity of a few characteristic Raman signals on the R6G concentration was analyzed *via* the calibration curve obtained in the plot of logarithmic values of various Raman peak intensity and R6G concentration in Fig. S3.† It can be noted from the calibration curve that the Raman intensities of R6G at 609 cm^{-1}, 769 cm^{-1}, 1175 cm^{-1} and 1307 cm^{-1} vary linearly with the R6G concentration. The linear fit to the data is shown as a solid red line. and the respective coefficient of determination, R^2, is given individually for each intensity plot. The R^2 values obtained were 0.91, 0.94, 0.90, 0.91 for the linear fitting of the peaks at 609, 769, 1175, and 1307 cm^{-1}, respectively, in the logarithmic plot of intensity *versus* R6G concentrations from 1 mM to 1 nM. The obtained R^2 values indicate good linearity with different Raman band intensity and concentration of R6G analyte. This confirms the

excellent consistent detection ability of the rGO-Ag-Bi_2O_3/$Bi_2O_{2.75}$ substrate towards the R6G dye. Further, the intensity plot for a few characteristic peaks of R6G for both the substrates rGO-Bi_2O_3/$Bi_2O_{2.75}$ and rGO-Ag-Bi_2O_3/$Bi_2O_{2.75}$ are shown in Fig. S4.† This clearly shows that the Ag-decked rGO-Bi_2O_3/$Bi_2O_{2.75}$ hybrid thin-film nanocomposite is an efficient substrate to detect R6G dye molecules.

3.4.1. Enhancement factor (*G*-factor) calculation. The enhancement factor (EF) or *G*-factor is a quantitative measure of the Raman signal enhancement of an analyte adsorbed on the SERS-active nanosubstrate under study. It also provides information about the sensitivity of the substrate towards the analyte. The EF for both the as-prepared hybrid thin film nanocomposite was determined using the equation given below:

$$\mathrm{EF} = \frac{I_{\mathrm{SERS}}}{I_{\mathrm{bulk}}} \times \frac{N_{\mathrm{bulk}}}{N_{\mathrm{SERS}}} \quad (2)$$

I_{SERS} is the Raman band intensity of R6G adsorbed on the SERS-active substrate under study. I_{bulk} is the intensity of the Raman signal recorded for the pure R6G analyte. As stated in our earlier report, R6G is a highly fluorescent dye; thus, we considered a 1 mM (10^{-3} M) concentration of R6G adsorbed on the glass substrate as the bulk.[60a] Here, we considered the intensity of the prominent SERS band at 772 cm^{-1} of R6G for the intensity ratio calculations. The $\frac{I_{\mathrm{SERS}}}{I_{\mathrm{bulk}}}$ ratio for R6G adsorbed on rGO-Bi_2O_3/$Bi_2O_{2.75}$ was determined to be ~8. The ratio of N_{bulk} to N_{SERS} was calculated as discussed by Z. Zhu *et al.*[61] N_{bulk} can be obtained using the following equation:

$$N_{\mathrm{bulk}} = \frac{Ah\rho}{m} \quad (3)$$

Here, A is the area of the laser spot (1.3 μm^2), h is the laser penetration depth (8.5 μm), and ρ and m are the density (1.26 g cm^{-3}) and molecular weight (479.02 g mol^{-1}) of R6G, respectively. N_{SERS} was determined using the equation established by Park *et al.*[62] The surface concentration in moles of 20 μL R6G for the lowest detected value for the rGO-Bi_2O_3/$Bi_2O_{2.75}$ substrate, *i.e.*, 10 μM, is 2×10^{-10} moles. Considering the product of the ratio of the number of molecules of R6G to the sampling area and area of the laser spot, N_{SERS} was calculated to be 3.28×10^{-18} moles. The intensity ratio and ratio of the number of molecules were substituted into eqn (2), and the enhancement factor was found to be 7×10^4, which is one order of magnitude greater than the EF values of 10^2 to 10^3 achieved for the rGO-MO SERS system in previous works. Similarly, the EF was calculated for the rGO-Ag-Bi_2O_3/$Bi_2O_{2.75}$ substrate with the lowest detection limit, which is a 10^{-9} M concentration of R6G. The intensity of the Raman peak at 769 cm^{-1} was considered for the intensity ratio calculation of I_{SERS} and I_{bulk} for the rGO-Ag-Bi_2O_3/$Bi_2O_{2.75}$ hybrid thin film nanocomposite substrate and was determined to be ~21. Here, the surface concentration in moles of 20 μL R6G for the lowest detected value in the case of rGO-Ag-Bi_2O_3/$Bi_2O_{2.75}$, *i.e.*, 1 nM, is 2×10^{-14} moles. Considering the product of the ratio of the number of molecules of R6G to the sampling area and area of the laser spot, N_{SERS} was determined to be 3.28×10^{-22} moles. Through substitution into eqn (2), the enhancement factor was determined to be 1.8×10^9. A five-fold increase in the EF was achieved after the incorporation of the Ag NPs in the rGO-Bi_2O_3/$Bi_2O_{2.75}$ nanocomposite.

3.4.2. SERS mechanism. Generally, the EF obtained for the rGO/MO SERS system in previous literature is of the order 10^2 due to a chemical enhancement mechanism (CE).[32] In addition to well-known SERS mechanisms such as electromagnetic enhancement (EM) and chemical enhancement (CE), oxygen vacancies and non-stoichiometric mediated defects in the nanostructure of metal oxide semiconductors have become recent key strategies for engineering SERS substrates for better enhancement.[16–18] The Raman signal enhancement in the semiconductors is mainly explained by applying the photo-induced charge transfer (PICT) mechanism along with molecular resonance, exciton resonance, and defect energy levels.[18] Pure Bi_2O_3 is a weak/non-SERS substrate, as shown in Fig. 11(c). However, in the rGO-Bi_2O_3/$Bi_2O_{2.75}$ hybrid substrate, the enhancement is due to the synergic effect of the charge transfer in rGO due to sp^2-enriched sites, and intrinsic oxygen vacancies generated in Bi_2O_{3-x} cause a Raman signal enhancement of up to 7×10^4 with a detection limit as low as 10^{-5} M for R6G. The further addition of a small amount of Ag to the hybrid nanocomposites gives a huge electromagnetic plasmonic enhancement, with an EF of 1.8×10^9 and lowest detection limit of 10^{-9} M for R6G. When the semiconductor Bi_2O_3/$Bi_2O_{2.75}$ adsorbs R6G molecules, it exerts charge transfer due to PICT. As per Herzberg–Teller theory, if the highest occupied molecular orbital (HOMO) and lowest unoccupied molecular orbital (LUMO) of the adsorbed molecule (R6G in this case) and incident photon excitation energy (532 nm = 2.33 eV) match the conduction band (CB) and valence band (VB) of the substrate (the semiconductor in this case), the PICT process occurs.[63] The HOMO and LUMO of the widely studied R6G molecule have been reported to be −5.70 eV and −3.40 eV, respectively.[17] Based on CB and VB values cited by Xu *et al.*, the SERS mechanism for rGO-Ag-Bi_2O_3/$Bi_2O_{2.75}$ after the adsorption of R6G is proposed, as shown in Fig. 13. The CB and VB values for Bi_2O_3 were calculated from bandgap values, which are calculated using density functional theory (DFT), whereas for $Bi_2O_{2.75}$, the CB and VB were obtained from Mulliken electronegativity theory by Xu *et al.*[23] As it is non-stoichiometric $Bi_2O_{2.75}$, their energy levels are shown separately, unlike for the presence of defects, which are considered as sub-state energy levels. We hypothesize that PICT is feasible from the Fermi energy level of Ag ($E_f = -4.84$ eV)[64] to the LUMO of the R6G molecule, as the energy difference between them is 1.44 eV, which is smaller than the incident laser source energy of 2.33 eV. The energy gap between the HOMO and LUMO of R6G is 2.35 eV, so there is a mild possibility of molecular resonance contributing to the SERS enhancement. PICT from the semiconductor to the molecule or from the molecule to the semiconductor is possible, as the energy difference between the VB of Bi_2O_3/$Bi_2O_{2.75}$ and the LUMO of R6G is 2.07 eV. Electron transition from the CB of Bi_2O_3 and the VB of $Bi_2O_{2.75}$ can also be feasible due to small energy difference of 0.26 eV between the two energy levels. Exciton resonance also contributes to the SERS signal enhancement due to the

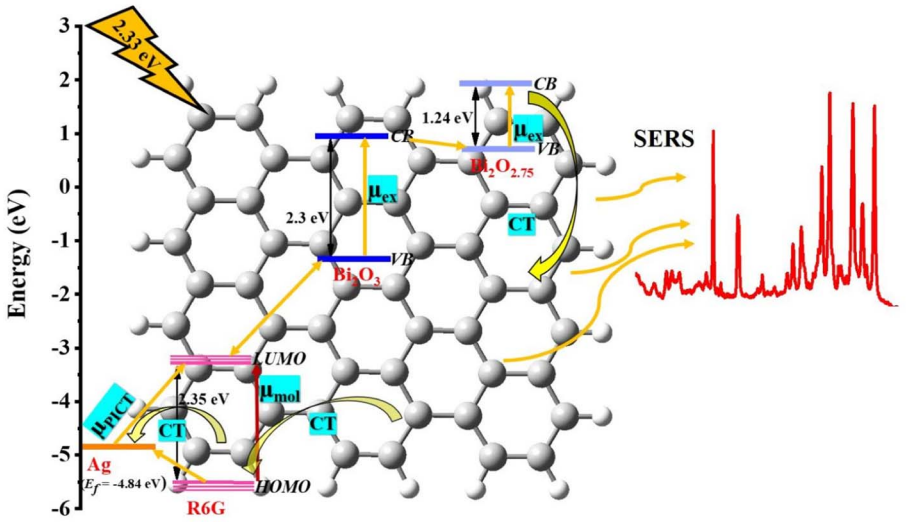

Fig. 13 Schematic of the proposed SERS mechanism for R6G adsorbed on rGO-Ag-Bi_2O_3/$Bi_2O_{2.75}$ hybrid thin-film nanocomposite.

formation and delocalization of the electron–hole pair formed after the excitation of an electron from the CB to the VB of Bi_2O_3 (E_g = 2.3 eV) and that of $Bi_2O_{2.75}$ (E_g = 1.24 eV). The electron transition pathway from the CB of Bi_2O_3/$Bi_2O_{2.75}$ to the HOMO of R6G is unavailable due to the large energy difference between the two energy levels. Further, R6G is conjugated and contains a benzene ring in its molecular structure, similar to that of graphene. When it is deposited on the rGO/Ag/Bi_2O_3/$Bi_2O_{2.75}$ hybrid thin-film nanocomposite, the vibrational signal of R6G is notably enhanced due to the π–π stacking. In addition, there is a key role of surface enhanced resonance Raman scattering (SERRS), especially in the case of R6G excited with a 532 nm laser. Based on coupled resonance theory, it has been proposed that certain vibrational modes obtain their intensity through a vibronic coupling mechanism.[60a,b,65] The EF achieved for rGO-Bi_2O_3/Bi_2O_{3-x} is of the order 10^4 due to the effective CT exhibited between the non-stoichiometric rGO-Bi_2O_3/Bi_2O_{3-x} hybrid thin film and R6G molecules as well as the SERRS effect of R6G upon illumination with a 532 nm laser. The further increase in EF for rGO-Ag-Bi_2O_3/Bi_2O_{3-x} is purely because of the strong plasmonic electromagnetic enhancement effect of the Ag NPs and viable electron transfer between the R6G molecules and Ag NPs. In our rGO-Ag-Bi_2O_3/Bi_2O_{3-x} substrate, the enhancement factor is better and comparable with that of the rGO-Ag substrate that was reported previously.[60a,66,67] Hence, the superior SERS enhancement in rGO-Ag-Bi_2O_3/$Bi_2O_{2.75}$ is due to the synergistic effect of the PICT among the non-stoichiometric rGO-Bi_2O_3/$Bi_2O_{2.75}$ system, plasmonic effect of Ag, molecular resonance or SERRS effect in R6G due to the excitation of 532 nm laser and exciton resonance in Bi_2O_3/$Bi_2O_{2.75}$.

4. Conclusions

We have the synthesized rGO-based, flower-like non-stoichiometric metal oxide hybrid thin-film nanocomposites rGO-Bi_2O_3/$Bi_2O_{2.75}$ and Ag-decked rGO-Ag-Bi_2O_3/$Bi_2O_{2.75}$ using a simple liquid/liquid interface (LLI) method. To the best of our knowledge, this is the first report of the preparation of non-stoichiometric metal oxide hybrids with rGO using the LLI method. The as-prepared non-stoichiometric rGO-Bi_2O_3/$Bi_2O_{2.75}$ and rGO-Ag-Bi_2O_3/$Bi_2O_{2.75}$ hybrid thin-film nanocomposites have been demonstrated to achieve effective detection of the hazardous dye R6G. The supporting characterization results confirm the morphological variation of rGO-Ag-Bi_2O_3/$Bi_2O_{2.75}$ and rGO-Bi_2O_3/$Bi_2O_{2.75}$ and the presence of the oxygen vacancies, which are responsible for the SERS enhancement of R6G. It is possible to achieve the detection of as little as 1 nM of R6G with an EF of 1.8 × 10^9 using the rGO-Ag-Bi_2O_3/$Bi_2O_{2.75}$ substrate; this represents an enhancement of more than five orders of magnitude compared to the rGO-Bi_2O_3/$Bi_2O_{2.75}$ hybrid substrate, which has an EF of 7 × 10^4. The stable and reproducible SERS spectrum of 1 mM R6G adsorbed on the rGO-Ag-Bi_2O_3/$Bi_2O_{2.75}$ substrate is shown in Fig. S5.† These substrates were prepared four to five times using the LLI method under identical conditions. Further, the substrates were stable and showed comparable sensitivity to the fresh substrate even three weeks after preparation. Fig. S6† shows the uniform and repeatable SERS spectra recorded on five different points on the same rGO-Ag-Bi_2O_3/$Bi_2O_{2.75}$ substrate. The improved SERS effect in the non-stoichiometric rGO-Ag-Bi_2O_3/$Bi_2O_{2.75}$ hybrid thin-film nanocomposite is due to the cumulative effect of the PICT process of the chemical mechanism in the non-stoichiometric rGO-Bi_2O_3/$Bi_2O_{2.75}$ system, the molecular resonance or vibronic coupled SERRS effect of R6G under 532 nm laser excitation, exciton resonance in Bi_2O_3/$Bi_2O_{2.75}$, electromagnetic enhancement due to the surface plasmon mechanism of the Ag NPs and the fluorescence-quenching nature of rGO. Hence, we propose the silver-decked flower-like non-stoichiometric hybrid thin-film nanocomposite rGO-Ag-Bi_2O_3/$Bi_2O_{2.75}$ as a highly sensitive SERS substrate for fluorescent dyes such as R6G. Further, we would like to explore these substrates for pesticides and biomolecules in the future.

Conflicts of interest

The authors declare no competing financial interest.

Acknowledgements

Dr C. K. thanks VGST-K-FIST-L2, GRD No. 937 for sponsored project funding. The authors acknowledge the Central Research Facilities at CeNS, Bengaluru and the SAMat Research Facilities at JNCASR, Bengaluru.

References

1 M. Liu, Z. Wang, S. Zong, H. Chen, D. Zhu, L. Wu, G. Hu and Y. Cui, SERS detection and removal of mercury (II)/silver (I) using oligonucleotide-functionalized core/shell magnetic silica sphere@ Au nanoparticles, *ACS Appl. Mater. Interfaces*, 2014, **6**(10), 7371–7379.

2 R. Gao, D. Li, Q. Zhang, S. Zheng, X. Ren and W. Deng, GNPs-QDs core–satellites assembly: trimodal platform for on-site identification and detection of TNT in complex media, *Sens. Actuators, B*, 2021, **328**, 128960.

3 R. Kanchanapally, S. S. Sinha, Z. Fan, M. Dubey, E. Zakar and P. C. Ray, Graphene oxide–gold nanocage hybrid platform for trace level identification of nitro explosives using a raman fingerprint, *J. Phys. Chem. C*, 2014, **118**(13), 7070–7075.

4 L. Wang, Z. F. Gan, D. Guo, H. L. Xia, F. T. Patrice, M. E. Hafez and D. W. Li, Electrochemistry-regulated recyclable SERS sensor for sensitive and selective detection of tyrosinase activity, *Anal. Chem.*, 2019, **91**(10), 6507–6513.

5 D. K. Boccorh, P. A. Macdonald, C. W. Boyle, A. J. Wain, L. E. Berlouis and A. W. Wark, A universal polymer shell-isolated nanoparticle (SHIN) design for single particle spectro-electrochemical SERS sensing using different core shapes, *Nanoscale Adv.*, 2021, **3**(22), 6415–6426.

6 W. A. El-Said, A. S. Al-Bogami and W. Alshitari, Synthesis of gold nanoparticles@ reduced porous graphene-modified ITO electrode for spectroelectrochemical detection of SARS-CoV-2 spike protein, *Spectrochim. Acta, Part A*, 2022, **264**, 120237.

7 K. M. Lee, D. Yarbrough, M. M. Kozman, T. J. Herrman, J. Park, R. Wang and D. Kurouski, Rapid detection and prediction of chlortetracycline and oxytetracycline in animal feed using surface-enhanced Raman spectroscopy (SERS), *Food Control*, 2020, **114**, 107243.

8 J. Zhuang, Z. Zhao, K. Lian, L. Yin, J. Wang, S. Man and L. Ma, SERS-based CRISPR/Cas assay on microfluidic paper analytical devices for supersensitive detection of pathogenic bacteria, *Biosens. Bioelectron.*, 2022, **207**, 114167.

9 S. W. Chook, C. H. Chia, C. H. Chan, S. X. Chin, S. Zakaria, M. S. Sajab and N. M. Huang, A porous aerogel nanocomposite of silver nanoparticles-functionalized cellulose nanofibrils for SERS detection and catalytic degradation of rhodamine B, *RSC Adv.*, 2015, **5**(108), 88915–88920.

10 Z. Gan, A. Zhao, M. Zhang, W. Tao, H. Guo, Q. Gao, R. Mao and E. Liu, Controlled synthesis of Au-loaded Fe_3O_4@C composite microspheres with superior SERS detection and catalytic degradation abilities for organic dyes, *Dalton Trans.*, 2013, **42**(24), 8597–8605.

11 Q. Cai, S. Lu, F. Liao, Y. Li, S. Ma and M. Shao, Catalytic degradation of dye molecules and *in situ* SERS monitoring by peroxidase-like Au/CuS composite, *Nanoscale*, 2014, **6**(14), 8117–8123.

12 A. Fălămaş, H. Rotaru and M. Hedeşiu, Surface-enhanced Raman spectroscopy (SERS) investigations of saliva for oral cancer diagnosis, *Laser Med. Sci.*, 2020, **35**(6), 1393–1401.

13 H. Li, Q. Wang, J. Tang, N. Gao, X. Yue, F. Zhong, X. Lv, J. Fu, T. Wang and C. Ma, Establishment of a reliable scheme for obtaining highly stable SERS signal of biological serum, *Biosens. Bioelectron.*, 2021, **189**, 113315.

14 M. Muhammad, C. S. Shao and Q. Huang, Aptamer-functionalized Au nanoparticles array as the effective SERS biosensor for label-free detection of interleukin-6 in serum, *Sens. Actuators, B*, 2021, **334**, 129607.

15 T. Moisoiu, S. D. Iancu, D. Burghelea, M. P. Dragomir, G. Iacob, A. Stefancu, R. G. Cozan, O. Antal, Z. Bálint, V. Muntean, R. I. Badea, E. Licarete, N. Leopold and F. I. Elec, SERS Liquid Biopsy Profiling of Serum for the Diagnosis of Kidney Cancer, *Biomedicines*, 2022, **10**(2), 233.

16 S. Cong, Y. Yuan, Z. Chen, J. Hou, M. Yang, Y. Su, Y. Zhang, L. Li, Q. Li, F. Geng and Z. Zhao, Noble metal-comparable SERS enhancement from semiconducting metal oxides by making oxygen vacancies, *Nat. Commun.*, 2015, **6**(1), 7800.

17 H. Wu, H. Wang and G. Li, Metal oxide semiconductor SERS-active substrates by defect engineering, *Analyst*, 2017, **142**(2), 326–335.

18 M. Chen, K. Li, Y. Luo, J. Shi, C. Weng, L. Gao and G. Duan, Improved SERS activity of non-stoichiometric copper sulfide nanostructures related to charge-transfer resonance, *Phys. Chem. Chem. Phys.*, 2020, **22**(9), 5145–5153.

19 B. Ramya Prabhu, C. Kavitha and N. S. John, Ag decorated sea urchin-MoO_3 based hierarchical micro-nanostructures as surface-enhanced Raman spectroscopy substrates for the detection of a nitrosamine industrial pollutant, *Mater. Today Commun.*, 2022, **33**, 104995.

20 M. M. Varier and N. S. John, Fabrication of sandwich structures of Ag/analyte/MoO_3 sea urchins for SERS detection of methylene blue dye molecules, *Nanotechnology*, 2023, **34**(21), 215701.

21 W. Fang, L. Zhou, B. Shen, Y. Zhou, Q. Yi, M. Xing and J. Zhang, Advanced $Bi_2O_{2.7}$/$Bi_2Ti_2O_7$ composite film with enhanced visible-light-driven activity for the degradation of organic dyes, *Res. Chem. Intermed.*, 2018, **44**, 4609–4618.

22 M. Wang, G. Tan, D. Zhang, B. Li, L. Lv, Y. Wang, H. Ren, X. Zhang, A. Xia and Y. Liu, Defect-mediated Z-scheme BiO_{2-x}/$Bi_2O_{2.75}$ photocatalyst for full spectrum solar-driven organic dyes degradation, *Appl. Catal., B*, 2019, **254**, 98–112.

23 X. Xu, Y. Wang, D. Zhang, J. Wang and Z. Yang, In situ growth of photocatalytic Ag-decorated β-Bi_2O_3/$Bi_2O_{2.7}$ heterostructure film on PVC polymer matrices with self-

cleaning and antibacterial properties, *Chem. Eng. J.*, 2022, **429**, 131058.

24 Y. Peng, K. K. Wang, T. Liu, J. Xu and B. G. Xu, Synthesis of one-dimensional Bi_2O_3-$Bi_2O_{2.33}$ heterojunctions with high interface quality for enhanced visible light photocatalysis in degradation of high-concentration phenol and MO dyes, *Appl. Catal., B*, 2017, **203**, 946–954.

25 L. C. Tien and S. H. Peng, Selective synthesis of α-Bi_2O_3/rGO and β-Bi_2O_3/rGO heterostructures as efficient visible-light-driven photocatalysts, *Ceram. Int.*, 2019, **45**(12), 15334–15342.

26 X. Liu, L. Pan, T. Lv, Z. Sun and C. Q. Sun, Visible light photocatalytic degradation of dyes by bismuth oxide-reduced graphene oxide composites prepared *via* microwave-assisted method, *J. Colloid Interface Sci.*, 2013, **408**, 145–150.

27 M. Jiang, Y. Ding, H. Zhang, J. Ren, J. Li, C. Wan, Y. Hong, M. Qi, B. Mei, L. Deng, Y. Wu, T. Han, H. Zhang and J. Liu, A novel ultrathin single-crystalline Bi_2O_3 nanosheet wrapped by reduced graphene oxide with improved electron transfer for Li storage, *J. Solid State Electrochem.*, 2020, **24**, 2487–2497.

28 L. Zhao, Y. Liu, X. Xi, Y. Shen, J. Wang, Y. Liu and Z. Nie, Bi/Bi_2O_3/WO_3 composite: A bifunctional plasmonic heterostructure for detection and degradation pollutions in wastewater, *J. Environ. Chem. Eng.*, 2022, **10**(3), 107643.

29 K. Ge, Y. Huang and H. Zhang, Fabrication of hierarchical β-Bi_2O_3/AuAg microspheres for sensitive, selective and rapid detection of environment pollutants by surface-enhanced Raman spectroscopy, *Spectrochim. Acta, Part A*, 2023, **285**, 121907.

30 R. Al-Gaashani, A. Najjar, Y. Zakaria, S. Mansour and M. A. Atieh, XPS and structural studies of high quality graphene oxide and reduced graphene oxide prepared by different chemical oxidation methods, *Ceram. Int.*, 2019, **45**(11), 14439–14448.

31 K. Bramhaiah and N. S. John, Hybrid films of reduced graphene oxide with noble metal nanoparticles generated at a liquid/liquid interface for applications in catalysis, *RSC Adv.*, 2013, **3**(21), 7765–7773.

32 K. Bramhaiah, V. N. Singh, C. Kavitha and N. S. John, Films of reduced graphene oxide with metal oxide nanoparticles formed at a liquid/liquid interface as reusable surface enhanced Raman scattering substrates for dyes, *J. Nanosci. Nanotechnol.*, 2017, **17**(4), 2711–2719.

33 C. Kim, D. H. Kim, J. S. Kim, Y. S. Han, J. S. Chung and H. Kim, A study of the synthesis of bismuth tellurium selenide nanocompounds and procedures for improving their thermoelectric performance, *J. Alloys Compd.*, 2011, **509**(39), 9472–9478.

34 M. Singh, R. Ramanathan, E. L. Mayes, S. Mašková, P. Svoboda and V. Bansal, One-pot synthesis of maghemite nanocrystals across aqueous and organic solvents for magnetic hyperthermia, *Appl. Mater. Today*, 2018, **12**, 250–259.

35 N. A. Devi, S. Sinha, S. Nongthombam and B. P. Swain, Structural, optical, electrochemical and electrical studies of Bi_2O_3@ rGO nanocomposite, *Mater. Sci. Semicond. Process.*, 2022, **137**, 106212.

36 L. Jiang, X. Yuan, G. Zeng, J. Liang, X. Chen, H. Yu, H. Wang, Z. Wu, J. Zhang and T. Xiong, In-situ synthesis of direct solid-state dual Z-scheme WO_3/g-C_3N_4/Bi_2O_3 photocatalyst for the degradation of refractory pollutant, *Appl. Catal., B*, 2018, **227**, 376–385.

37 Y. Liu, F. Xin, F. Wang, S. Luo and X. Yin, Synthesis, characterization, and activities of visible light-driven Bi_2O_3–TiO_2 composite photocatalysts, *J. Alloys Compd.*, 2010, **498**(2), 179–184.

38 G. H. Jiang, X. Li, Z. Wei, T. T. Jiang, X. X. Du and W. X. Chen, Effects of N and/or S doping on structure and photocatalytic properties of BiOBr crystals, *Acta Metall. Sin. (Engl. Lett.)*, 2015, **28**, 460–466.

39 S. Singh, R. K. Sahoo, N. M. Shinde, J. M. Yun, R. S. Mane, W. Chung and K. H. Kim, Asymmetric faradaic assembly of Bi_2O_3 and MnO_2 for a high-performance hybrid electrochemical energy storage device, *RSC Adv.*, 2019, **9**(55), 32154–32164.

40 T. Kar, S. Scheiner, U. Adhikari and A. K. Roy, Site preferences of carboxyl groups on the periphery of graphene and their characteristic IR spectra, *J. Phys. Chem. C*, 2013, **117**(35), 18206–18215.

41 S. E. Wiberley and R. D. Gonzalez, Infrared spectra of polynuclear aromatic compounds in the CH stretching and out-of-plane bending regions, *Appl. Spectrosc.*, 1961, **15**(6), 174–177.

42 R. P. Dighole, A. V. Munde, B. B. Mulik and B. R. Sathe, Bi_2O_3 nanoparticles decorated carbon nanotube: an effective nanoelectrode for enhanced electrocatalytic 4-nitrophenol reduction, *Front. Chem.*, 2020, **8**, 325.

43 D. Li, M. B. Müller, S. Gilje, R. B. Kaner and G. G. Wallace, Processable aqueous dispersions of graphene nanosheets, *Nat. Nanotechnol.*, 2008, **3**(2), 101–105.

44 L. Shan, G. Wang, D. Li, X. San, L. Liu, L. Dong and Z. Wu, Band alignment and enhanced photocatalytic activation of α/β-Bi_2O_3 heterojunctions *via in situ* phase transformation, *Dalton Trans.*, 2015, **44**(17), 7835–7843.

45 Y. Li, M. Wen, Y. Wang, G. Tian, C. Wang and J. Zhao, Plasmonic Hot Electrons from Oxygen Vacancies for Infrared Light-Driven Catalytic CO_2 Reduction on Bi_2O_{3-x}, *Angew. Chem.*, 2021, **133**(2), 923–929.

46 Y. Li, Z. Zhang, Y. Zhang, X. Sun, J. Zhang, C. Wang, Z. Peng and H. Si, Preparation of Ag doped Bi_2O_3 nanosheets with highly enhanced visible light photocatalytic performances, *Ceram. Int.*, 2014, **40**(8), 13275–13280.

47 S. Malynych and G. Chumanov, Light-induced coherent interactions between silver nanoparticles in two-dimensional arrays, *J. Am. Chem. Soc.*, 2003, **125**(10), 2896–2898.

48 L. M. Malard, M. A. Pimenta, G. Dresselhaus and M. S. Dresselhaus, Raman spectroscopy in graphene, *Phys. Rep.*, 2009, **473**(5–6), 51–87.

49 D. López-Díaz, M. Lopez Holgado, J. L. García-Fierro and M. M. Velázquez, Evolution of the Raman spectrum with

the chemical composition of graphene oxide, *J. Phys. Chem. C*, 2017, **121**(37), 20489–20497.

50 A. C. Ferrari, Raman spectroscopy of graphene and graphite: Disorder, electron–phonon coupling, doping and nonadiabatic effects, *Solid State Commun.*, 2007, **143**(1–2), 47–57.

51 A. C. Ferrari and J. Robertson, Interpretation of Raman spectra of disordered and amorphous carbon, *Phys. Rev. B: Condens. Matter Mater. Phys.*, 2000, **61**(20), 14095.

52 M. M. Shahid, P. Rameshkumar, A. Pandikumar, H. N. Lim, Y. H. Ng and N. M. Huang, An electrochemical sensing platform based on a reduced graphene oxide–cobalt oxide nanocube@platinum nanocomposite for nitric oxide detection, *J. Mater. Chem. A*, 2015, **3**(27), 14458–14468.

53 P. Cui, J. Lee, E. Hwang and H. Lee, One-pot reduction of graphene oxide at subzero temperatures, *Chem. Commun.*, 2011, **47**(45), 12370–12372.

54 X. N. He, Y. Gao, M. Mahjouri-Samani, P. N. Black, J. Allen, M. Mitchell and Y. F. Lu, Surface-enhanced Raman spectroscopy using gold-coated horizontally aligned carbon nanotubes, *Nanotechnology*, 2012, **23**(20), 205702.

55 G. Lin, D. Tan, F. Luo, D. Chen, Q. Zhao, J. Qiu and Z. Xu, Fabrication and photocatalytic property of α-Bi_2O_3 nanoparticles by femtosecond laser ablation in liquid, *J. Alloys Compd.*, 2010, **507**(2), L43–L46.

56 Z. Deng, T. Liu, T. Chen, J. Jiang, W. Yang, J. Guo, J. Zhao, H. Wang and L. Gao, Enhanced electrochemical performances of Bi_2O_3/rGO nanocomposite *via* chemical bonding as anode materials for lithium ion batteries, *ACS Appl. Mater. Interfaces*, 2017, **9**(14), 12469–12477.

57 R. Bhujel, S. Rai, Z. Mustafa, G. Sarkar, U. Deka, J. Biswas and B. P. Swain, Synthesis and characterization of graphene sheet decorated with silver nanoparticles. in *AIP Conference Proceedings*, AIP Publishing LLC, 2020, November, vol. 2273, No. 1, p. 040002.

58 G. Upender, R. Satyavathi, B. Raju, K. S. Alee, D. N. Rao and C. Bansal, Silver nanocluster films as novel SERS substrates for ultrasensitive detection of molecules, *Chem. Phys. Lett.*, 2011, **511**(4–6), 309–314.

59 G. Li, H. Li, Y. Mo, X. Huang and L. Chen, Surface enhanced resonance Raman spectroscopy of rhodamine 6G adsorbed on silver electrode in lithium batteries, *Chem. Phys. Lett.*, 2000, **330**(3–4), 249–254.

60 (*a*) C. Kavitha, K. Bramhaiah, N. S. John and B. E. Ramachandran, Low cost, ultra-thin films of reduced graphene oxide–Ag nanoparticle hybrids as SERS based excellent dye sensors, *Chem. Phys. Lett.*, 2015, **629**, 81–86; (*b*) J. R. Lombardi, R. L. Birke and G. Haran, Single Molecule SERS Spectral Blinking and Vibronic Coupling, *J. Phys. Chem. C*, 2011, **115**, 4540–4545.

61 Z. Zhu, T. Zhu and Z. Liu, Raman scattering enhancement contributed from individual gold nanoparticles and interparticle coupling, *Nanotechnology*, 2004, **15**(3), 357.

62 H. K. Park, J. K. Yoon and K. Kim, Novel fabrication of Ag thin film on glass for efficient surface-enhanced Raman scattering, *Langmuir*, 2006, **22**(4), 1626–1629.

63 X. Wang, W. Shi, G. She and L. Mu, Surface-Enhanced Raman Scattering (SERS) on transition metal and semiconductor nanostructures, *Phys. Chem. Chem. Phys.*, 2012, **14**(17), 5891–5901.

64 Z. Xiaolei, Y. Zhi, J. Wei, S. Huimin, C. Qian, W. Xu and Z. Bing, Charge-Transfer Effect on Surface-Enhanced Raman Scattering (SERS) in an Ordered Ag NPs/4-Mercaptobenzoic Acid/TiO_2 System, *J. Phys. Chem. C*, 2015, **119**(39), 22439–22444.

65 T. Vosgröne and A. J. Meixner, Surface and resonance enhanced micro-Raman spectroscopy of xanthene dyes at the single-molecule level, *J. Lumin.*, 2004, **107**(1–4), 13–20.

66 A. K. Nair, K. B. Bhavitha, S. Perumbilavil, P. Sankar, D. Rouxel, M. S. Kala, S. Thomas and N. Kalarikkal, Multifunctional nitrogen sulfur co-doped reduced graphene oxide–Ag nano hybrids (sphere, cube and wire) for nonlinear optical and SERS applications, *Carbon*, 2018, **132**, 380–393.

67 Q. Hong, L. Jiang, S. Wang, J. Huang, J. Sun, X. Li, P. Zuo, J. Yin and J. Lu, One-Step *In Situ* Patternable Reduction of a Ag–rGO Hybrid Using Temporally Shaped Femtosecond Pulses, *Materials*, 2022, **15**(2), 563.